

Discovery of synchronous X-ray & radio moding of PSR B0823+26

W. Hermsen^{1,2}, L. Kuiper¹, R. Basu^{4,7}, J.W.T. Hessels^{2,3}, D. Mitra^{4,5,7}, J.M. Rankin^{2,5}, B.W. Stappers⁶, G.A.E. Wright⁶, J.-M. Grießmeier^{9,8}, M. Serylak^{10,11,8}, A. Horneffer¹², C. Tiburzi^{12,13}, W.C.G. Ho^{14,15}

¹*SRON Netherlands Institute for Space Research, Sorbonnelaan 2, 3584 CA Utrecht, The Netherlands.*

²*Anton Pannekoek Institute for Astronomy, University of Amsterdam, Science Park 904, 1098 XH, Amsterdam, The Netherlands.*

³*ASTRON, the Netherlands Institute for Radio Astronomy, Postbus 2, 7990 AA, Dwingeloo, The Netherlands.*

⁴*National Centre for Radio Astrophysics, (NCFRA-TIFR), Post Bag 3, Ganeshkhind, Pune University Campus, Pune 411007, India.*

⁵*Physics Department, University of Vermont, Burlington, VT 05405, USA.*

⁶*Jodrell Bank Centre for Astrophysics, School of Physics and Astronomy, University of Manchester, Manchester M13 9PL, UK.*

⁷*Janusz Gil Institute of Astronomy, University of Zielona Góra, Lubuska 2, PL-65-265 Zielona Góra, Poland.*

⁸*Station de Radioastronomie de Nançay, Observatoire de Paris, CNRS, PSL Research University, Univ. d'Orléans, F-18330 Nançay, France.*

⁹*LPC2E - Université d'Orléans, CNRS, 45071 Orléans, France*

¹⁰*SKA South Africa, The Park, Park Road, Pinelands 7405, South Africa*

¹¹*Department of Physics & Astronomy, University of the Western Cape, Private Bag X17, Bellville 7535, South Africa.*

¹²*Max-Planck-Institut für Radioastronomie, Auf dem Hügel 69, 53121 Bonn, Germany.*

¹³*Fakultät für Physik, Universität Bielefeld, Postfach 100131, 33501 Bielefeld, Germany.*

¹⁴*Mathematical Sciences, Physics & Astronomy and STAG Research Centre, University of Southampton, Southampton, SO17 1BJ, UK*

¹⁵*Department of Physics and Astronomy, Haverford College, 370 Lancaster Avenue, Haverford, PA 19041, USA*

Accepted 2018 July 30. Received 2018 July 09; in original form 2018 May 28.

ABSTRACT

Simultaneous observations of PSR B0823+26 with ESA's *XMM-Newton*, the Giant Metre-wave Radio Telescope and international stations of the Low Frequency Array revealed synchronous X-ray/radio switching between a radio-bright (B) mode and a radio-quiet (Q) mode. During the B mode we detected PSR B0823+26 in 0.2–2 keV X-rays and discovered pulsed emission with a broad sinusoidal pulse, lagging the radio main pulse by 0.208 ± 0.012 in phase, with high pulsed fraction of 70–80%. During the Q mode PSR B0823+26 was not detected in X-rays (2σ upper limit a factor ~ 9 below the B-mode flux). The total X-ray spectrum, pulse profile and pulsed fraction can globally be reproduced with a magnetized partially ionized hydrogen atmosphere model with three emission components: a primary small hot spot ($T \sim 3.6 \times 10^6$ K, $R \sim 17$ m), a larger cooler concentric ring ($T \sim 1.1 \times 10^6$ K, $R \sim 280$ m) and an antipodal hot spot ($T \sim 1.1 \times 10^6$ K, $R \sim 100$ m), for the angle between the rotation axis and line of sight direction $\sim 66^\circ$. The latter is in conflict with the radio derived value of $(84 \pm 0.7)^\circ$. The average X-ray flux within hours-long B-mode intervals varied by a factor $\pm 20\%$, possibly correlated with variations in the frequency and lengths of short radio nulls or short durations of weak emission. The correlated X-ray/radio moding of PSR B0823+26 is compared with the anti-correlated moding of PSR B0943+10, and the lack of X-ray moding of PSR B1822–09. We speculate that the X-ray/radio switches of PSR B0823+26 are due to variations in the rate of accretion of material from the interstellar medium through which it is passing.

Key words: stars: neutron — pulsars: general — Radio continuum: individual: PSR B0823+26 — X-rays: individual: PSR B0823+26, PSR B0943+10, PSR B1822–09

1 INTRODUCTION

So far, synchronous X-ray and radio mode switching has only been observed for the old and nearly aligned PSR B0943+10 (Hermsen et al. 2013). When this paragon of pulsar-mode switching (Sulejmanova & Izvekova 1984; Rankin & Sulejmanova 2006) switches from a radio “bright” (B) mode to a radio “quiet” (Q)

mode, the X-ray flux increases by a factor of ~ 2.4 and the X-ray pulsed fraction changes in magnitude and as a function of energy (Mereghetti et al. 2016). The results are broadly consistent with the predictions of the partially screened gap model for rotation-powered pulsar emission (e.g. Szary et al. (2015)), but they might also imply global magnetospheric rearrangements to explain the mode switching, as proposed in studies of intermittent

pulsars (Kramer et al. 2006; Lyne et al. 2010; Camilo et al. 2012; Lorimer et al. 2012). It is imperative to find other moding pulsars in which this phenomenon can be precisely characterised and the results compared with PSR B0943+10.

In a first attempt to find another example, we have conducted a similar campaign on the radio mode-switching pulsar PSR B1822–09 (Fowler et al. 1981; Fowler & Wright 1982). This pulsar exhibits mode switching on timescales of minutes, much shorter than the characteristic timescale of hours seen for PSR B0943+10. We found no evidence for simultaneous radio/X-ray mode switching of PSR B1822–09 (Hermsen et al. 2017). Though, we did, surprisingly, find a correlation between the mode durations and regular modulations in the pulse intensity. For this pulsar, it is possible that the very different geometry between the magnetic and spin axes (nearly orthogonal) may be hiding any visible X-ray mode changes, or that the physics of the short moding is quite different.

In this work we report on a new observational campaign targeting the moding pulsar PSR B0823+26. This pulsar is one of the brightest radio pulsars in the Northern sky, located at a distance of only ~ 320 pc. It has a period P of ~ 530 ms, a spin-down age of $\sim 4.9 \times 10^6$ yr and an inferred magnetic field of $\sim 9.8 \times 10^{11}$ G. It is by no means an ordinary pulsar, showing main-pulse, inter-pulse and post-cursor emission components (Backer et al. 1973). The pulsar was found to exhibit nulling (i.e. abrupt cessation and re-activation of its radio emission; see e.g. Rathnasree & Rankin (1995). More recently Young et al. (2012)) found the nulls to be both short-term (\sim min) as well as unusually long-term (\sim hours or more). During bursts in its B mode PSR B0823+26 was found to exhibit single-pulse modulations with a repetition period $P_3 \sim 5P$ (Backer 1973; Weltevrede et al. 2006b, 2007). Sobey et al. (2015) reported the discovery with LOFAR of a very weak quiet (Q) emission mode during these apparent nulling intervals. The transition between the Q mode and B mode occurs simultaneously for the main pulse, inter-pulse and post-cursor within about a single rotation of the neutron star. From the latter work we estimate the pulsar to be in the Q/null mode for $\sim 30\%$ of the time and the remaining $\sim 70\%$ in the B mode.

PSR B0823+26 was also detected with *XMM-Newton* in X-rays in April 2002 (Becker et al. 2004), with an effective EPIC Pn exposure of 33.7 ks. The detected source count rate in the Pn CCD was 3.5×10^{-3} counts s^{-1} for energies 0.3–10 keV, or an X-ray luminosity (0.5–10 keV) of $\sim 1.0 \times 10^{29}$ erg s^{-1} . Furthermore, there was a 2.2σ indication for the detection of a pulsed signal. Considerably more exposure is apparently required to confirm the indication for pulsed emission, as well as for significantly constraining the spectral parameters of the X-ray emission.

We carried out an X-ray/radio campaign on PSR B0823+26 with 6×25 ks of *XMM-Newton* observations, and simultaneous radio observations primarily with the GMRT at 325 MHz, supported by LOFAR UK, FR, SE and DE International stations in standalone mode at 150 MHz. From Lovell Telescope radio monitoring of PSR B0823+26 we derived an ephemeris to facilitate phase folding of the arrival times of the X-ray events.

In Section 2, we present the radio observations and how we defined the radio modes. In the subsequent sections, we present the *XMM-Newton* X-ray observations (Section 3), the spatial analysis of the sky maps for the six X-ray observations, leading to the discovery of synchronous X-ray/radio mode switching (Section 4), the first detection of the X-ray pulsed signal from PSR B0823+26 (Section 5), followed by the spectral characterisation of the total and pulsed emissions (Section 6). In Section 7, we sum-

Table 1. Radio observations of PSR B0823+26 in April 2017 with the GMRT and the LOFAR DE601 International Telescope (Effelsberg), together covering most of the simultaneous observations with *XMM-Newton* (Table 2). For definitions of the radio Bright (B), Null, Quiet (Q) and Q-bright mode, see text.

Telesc.	Date (yyyy-mm-dd)	Freq. (MHz)	Start (UT) (hh:mm)	End (UT) (hh:mm)	Radio mode
GMRT	2017-04-20	325	08:23	16:30	B
	2017-04-22	325	08:14	13:20	B
	2017-04-24	325	08:06	09:03	Null
	2017-04-24	325	09:03	09:10	Q-bright
	2017-04-24	325	09:10	16:24	Q
	2017-04-26	325	12:30	16:30	B
	2017-04-28	325	09:26	16:05	B
	2017-04-30	325	09:03	12:59	B
LOFAR	2017-04-20	150	12:46	22:49	B
	2017-04-22	150	12:38	22:44	B
	2017-04-24	150	12:45	17:00	Q
	2017-04-24	150	17:00	22:39	B
	2017-04-26	150	12:22	22:26	B
	2017-04-28	150	12:14	21:48	B
	2017-04-28	150	21:48	22:18	Q
	2017-04-30	150	15:27	22:07	B

marise our findings, followed in Section 8 by a discussion of them in comparison with the results from the previous campaigns on PSR B0943+10 and PSR B1822–09. Finally, our overall conclusions are presented in Section 10.

2 RADIO OBSERVATIONS AND MODE DETERMINATIONS

Due to orbital viewing constraints of *XMM-Newton*, simultaneous radio coverage of our X-ray observations of PSR B0823+26 in 2017 could mainly be realised with the GMRT, with support by LOFAR international stations for the last part of each assigned orbit of the space craft. In those cases when there was a mismatch in the scheduled *XMM-Newton* / GMRT observations, or when the GMRT encountered operational problems, the LOFAR observations could provide the required information for our analysis.

2.1 GMRT

Simultaneous radio/X-ray observations of PSR B0823+26 were carried out at the GMRT for six observing sessions of ~ 7.5 h each in 2017 April at 325 MHz (see Table 1). The GMRT is a multi-element aperture synthesis telescope (Swarup et al. 1991). The observations discussed here were done in a similar manner as discussed in (Hermsen et al. 2017). To maximize the sensitivity for single pulse detection in our study, we used approximately twenty antennas in the phased array, including all the available central square antennas and the two nearest arm antennas. The observing strategy was to do “phasing” of the array using a strong nearby phase calibrator and then observe the pulsar in an interlaced manner. To avoid dephasing due for long observations the phasing of the array was done every 1.5 hours, which however caused missing

data in the pulsar time sequence for a few minutes. We used a total bandwidth of about 33 MHz in the frequency range 306–339 MHz, spread over 256 channels. The data were recorded in the filter-bank format with time resolution of 0.122 ms, which was subsequently averaged to 0.488 ms.

The observing sessions were scheduled such that there was substantial overlap with the *XMM-Newton* observations. Generally, GMRT commenced the observations later than *XMM-Newton* by 18 minutes up to ~ 1 hour (compare Table 1 with Table 2). On April 26 the GMRT encountered problems and started 6 hours 46 minutes later than *XMM-Newton*, unfortunately. On two occasions, April 22 and 30, GMRT stopped observing earlier than *XMM-Newton*, by 2 hours 24 minutes and 3 hours 1 minute, respectively. The latter time intervals were covered with the LOFAR international stations (see below).

At GMRT frequencies, PSR B0823+26 is a strong radio source and the main pulse (MP) can be used to readily identify mode switches. Very similar to the classification used by Sobey et al. (2015), we defined in this work the following radio modes, :

1) B mode: in this mode the pulsar is bright and displays short (a few pulses) nulls (cessation of emission). The main pulse (MP), the pre-cursor (PC) and the inter-pulse (IP) can be easily seen, though the IP at 325 MHz is weak.

2) Null mode: the pulsar nulls in this mode and the average phase distribution does not show pulsed emission. Some sporadic spiky single-pulse emission across the mode cannot be ruled out.

3) Q mode: in the Q mode the pulsar shows sporadic and spiky single pulse emission in the region around the MP, including short nulls. The PC and IP are not seen at 325 MHz in this mode. This is consistent with Sobey et al. (2015), who called this behaviour RRAT-like.

4) Q-bright mode: in the Q mode we detected the onset of the mode to be associated with a bright sequence where both MP and PC can be seen, and the mode gradually fades to the Q mode.

Fig. 1 shows an example of PSR B0823+26 detected in B mode. It shows 22 minutes of single-pulse sequences of the MP measured with the GMRT at 325 MHz in our first observation. Unexpectedly, during five of our GMRT observations lasting on average ~ 7.5 h PSR B0823+26 appeared to be continuously in the B mode (see Table 1). Only in the observation on 2017 April 24 was PSR B0823+26 predominantly in the Q mode. In fact, the observations started when PSR B0823+26 was in the Null mode, then entered briefly the Q-bright mode and faded into the Q mode for the rest of the observation. These transitions are shown for the MP in Fig. 2. The Q-bright mode lasted only ~ 6 -7 minutes, and the average pulse energy is lower by a factor 7-10 than the average measured in the B mode.

2.2 LOFAR

For our campaign we were assigned 6×9 hours of observations at 150 MHz with the LOFAR (Stappers et al. 2011; van Haarlem et al. 2013) DE601, FR606, SE607 and UK608 international stations in stand-alone mode (as part of project LC7-014), partly simultaneous with *XMM-Newton*. The stations provided redundancy and backup in the case of problems, also with the GMRT observations, and co-adding them incoherently can boost the S/N by a factor of ~ 2 . It was only possible for the LOFAR observations to be simultaneous with *XMM-Newton* and GMRT for the last hours of each of the *XMM-Newton* observations. Table 1 lists the observation times with the LOFAR DE601 international telescope, representative for the

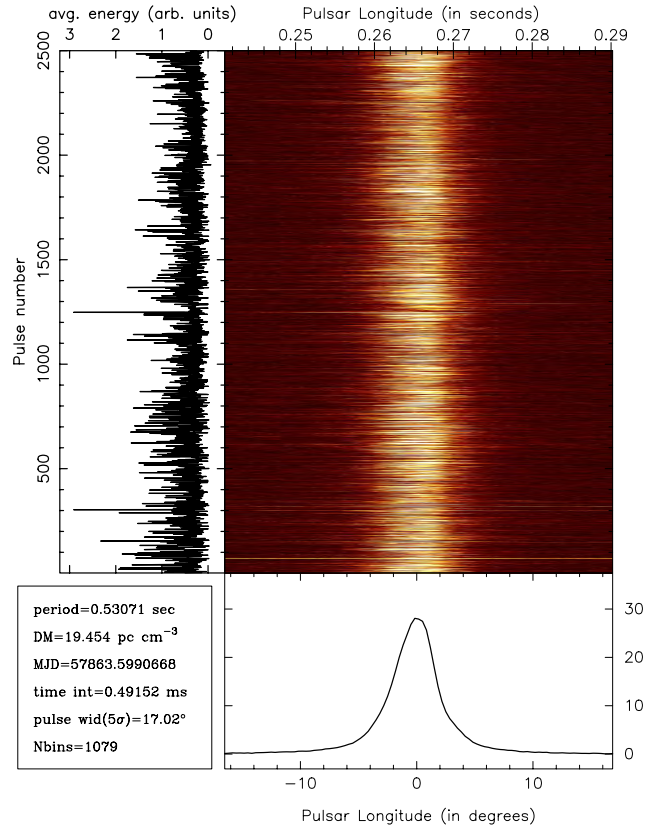


Figure 1. GMRT observation at 325 MHz of PSR B0823+26 on 2017 April 20, showing as a typical example PSR B0823+26 in B mode during 2500 single-pulse sequences, or ~ 22 minutes of the total duration of ~ 7.5 hours in B mode. Observation time versus pulsar phase centred on the main pulse with underneath the integrated profile of the main pulse, and to the left the average energy per pulse in arbitrary units.

observations with all participating LOFAR international stations. During all simultaneous GMRT and LOFAR observations there was agreement about the assigned radio mode of PSR B0823+26. On April 22 and 30, the GMRT observations ended before the end of the *XMM-Newton* observations by ~ 3 hours. In both cases LOFAR showed that PSR B0823+26 continued in the B mode for the remainder of the *XMM-Newton* observations. In Table 1 one can see that LOFAR measured two mode transitions, Q to B mode on April 22, and B to Q mode on April 28, 2017. Unfortunately, these transitions were not covered by *XMM-Newton*.

3 XMM-NEWTON X-RAY OBSERVATIONS

In April 2017, we obtained six *XMM-Newton* observations of PSR B0823+26 with durations between ~ 7 and 9.5 h (see Table 2). We used only data obtained with the EPIC instrument aboard *XMM-Newton*, which consists of one camera based on Pn CCDs (Strüder et al. 2001), the Pn, and two cameras based on MOS CCDs (Turner et al. 2001), MOS 1 and MOS 2. The Pn camera was operated in Large Window mode, which provides a time resolution of 47.7 ms, and the MOS cameras in Small Window mode with a time resolution of 300 ms. The latter time resolution is insufficient for timing studies of PSR B0823+26 with its period of 530 ms. For the

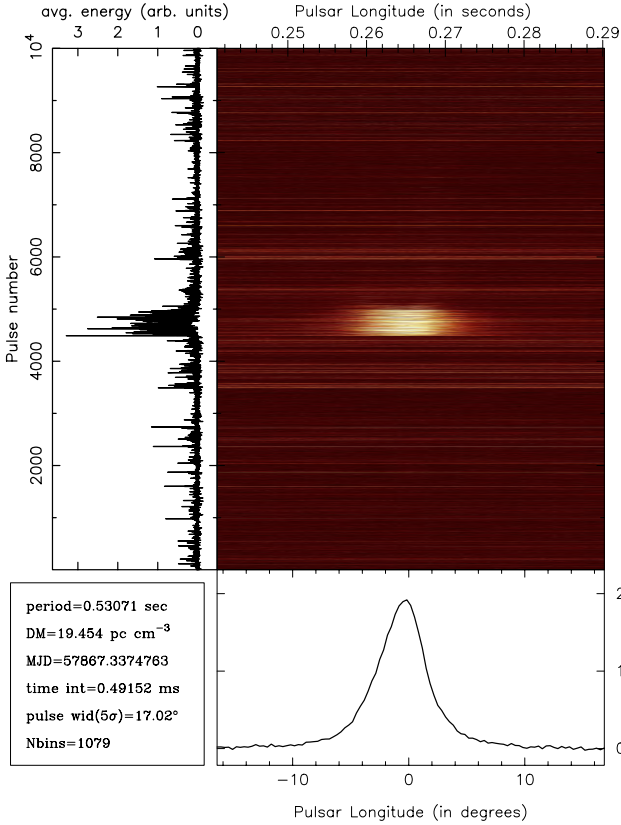


Figure 2. GMRT observation at 325 MHz of PSR B0823+26 on 2017 April 24, showing the first 10,000 single-pulse sequences, or ~ 88 minutes of the total ~ 7.5 hours of observation time. For explanation of figures, see caption of Fig. 1. The pulsar starts in the Null mode at pulse number 0, switches into the Q-bright mode around pulse number 4500 and decays into the Q mode for the rest of the observation around pulse number 5250. Note: the energy scale of the pulses is arbitrary, and in this figure almost an order of magnitude smaller than that in Fig. 1. An almost identical event can be seen in Fig. 3 of Sobey et al. (2015).

Table 2. *XMM-Newton* observation times of our six observations of PSR B0823+26 in 2017 April with the Pn and MOS cameras. Observation IDs 078440-0701, -0801, -0901, -1001, -1101, -1201, from top to bottom. The last column lists the dead-time-corrected exposures (lifetimes) per observation and for the total. The values listed for MOS apply to MOS 1 and MOS 2.

Date yyyy-mm-dd	Start Pn/MOS hh:mm (UT)	End Pn/MOS hh:mm (UT)	Exp. Pn/MOS [ks]
2017-04-20	07:28 / 06:59	16:07 / 16:06	28.4 / 31.2
2017-04-22	07:22 / 06:54	14:38 / 14:38	23.6 / 24.0
2017-04-24	06:54 / 06:26	14:10 / 14:10	23.8 / 26.4
2017-04-26	06:43 / 06:15	16:14 / 16:14	31.3 / 34.2
2017-04-28	08:38 / 08:10	15:54 / 15:53	23.8 / 26.5
2017-04-30	08:44 / 08:16	16:00 / 16:00	23.8 / 26.6
Total			154.7 / 168.9

three cameras we used the thin optical filter. We verified that our observations were not affected by increased particle backgrounds due to soft proton flares. The total lifetime (dead time corrected exposure) for the Pn and MOS cameras are also given in Table 2. The radio observations covered $\sim 87\%$ of the total *XMM-Newton* observations.

4 X-RAY SPATIAL ANALYSIS AND MODE SWITCHING

In the spatial analysis, we apply a two-dimensional Maximum Likelihood (ML) method to the EPIC Pn and MOS 1 and 2 data using our knowledge of the two-dimensional point-source signature (the point spread function; PSF), and taking into account the Poissonian nature of the counting process. At first the events¹ are sorted in two-dimensional count sky maps. The PSF is fitted to this count distribution at the known position of the pulsar on top of a background structure, assumed to be flat. Typical fit-region sizes are of the order of $30\text{--}60''$. For further details of the ML analysis that we applied to the EPIC Pn and MOS 1 and 2 data (treating these separately), see Hermsen et al. (2017).

Given the detection with *XMM-Newton* of PSR B0823+26 by Becker et al. (2004) and assuming that PSR B0823+26 behaves as a stable emitter in X-rays, we expected to detect the pulsar in each of the six separate observations in the raw detector images. In the first step of the analysis we produced for each observation such raw detector images for energies $0.5\text{--}2$ keV, and surprisingly already obtained convincing evidence of synchronous X-ray/radio mode switching of PSR B0823+26. In the maps of the five observations during which the pulsar was shown to be in the radio-B mode, indeed, the pulsar was clearly visible, however, for the radio-Q-mode observation on April 24 the source was not visible in the raw images. Fig. 3 shows as an example the raw images for the EPIC Pn detector, energies $0.5\text{--}2$ keV, for the observations on April 22, 24 and 26. Application of the ML analysis to the calibrated data of the radio B-mode observations, including energies down to 0.2 keV, rendered detection significances (energies $0.2\text{--}2$ keV) ranging from 11.7σ to 19.2σ . For the observation on April 24, including the short Q-bright mode, the ML analysis showed a much weaker 3.0σ detection for a similar exposure.

In order to investigate this further, we show in Fig. 4 the pulsar count rates ($0.2\text{--}2$ keV) in time intervals of ~ 1 hour for all our observations. It is evident that the X-ray count rate gives a direct indication of the actual radio B or Q mode of PSR B0823+26. Furthermore, Fig. 4 shows that the X-ray count rates at the start of each observation where we did not have radio coverage, are consistent with the values measured during the rest of the observations, whether PSR B0823+26 is then in the B mode or the Null or Q mode. Therefore, we can conclude that PSR B0823+26 was at the start of the observations on April 20, 22, 26, 28 and 30 already in the radio B mode, and on April 24 in the radio Null or Q mode. We have adopted this classification in the further X-ray analysis when selecting X-ray events in observation windows with PSR B0823+26 in the radio B or Q mode.

One can see in Fig. 4 that during the Q-mode observation six of the seven flux values are within $1\text{--}2\sigma$ consistent with no detection. Only one value stands out significantly. Selecting the data

¹ Each event i is characterised by its (barycentred) arrival time t_i , spatial coordinates x_i, y_i , energy E_i , event pattern ξ_i and flag F_i . We used $\xi_i = [0, 4]$ and flag $F_i = 0$ for both Pn and MOS.

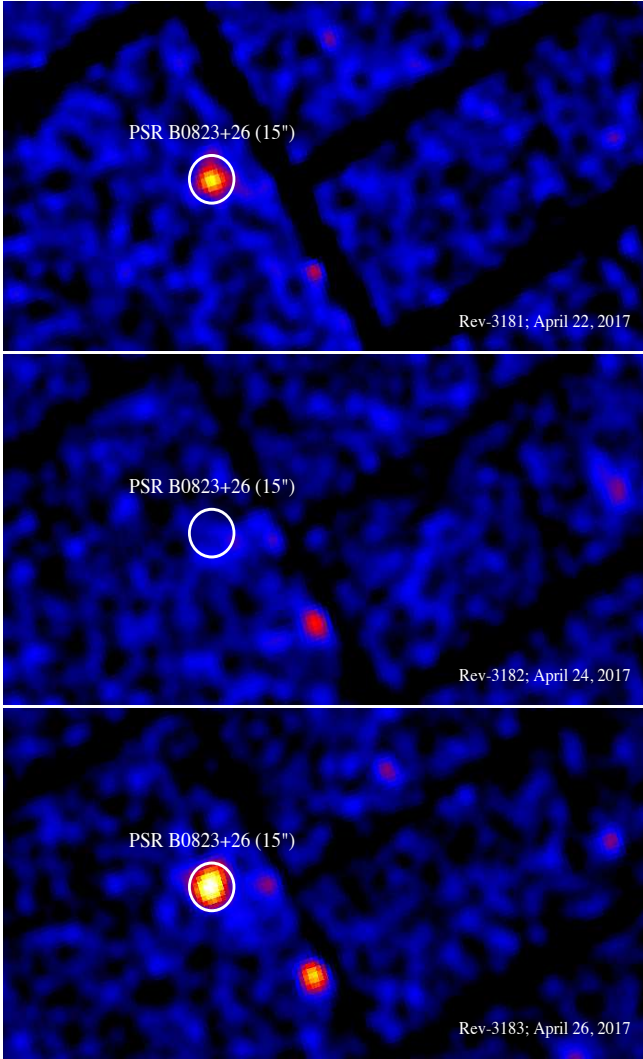


Figure 3. *XMM-Newton* EPIC Pn raw detector images (dimensions ~ 7 by 4 arcmin) in celestial coordinates ($\alpha_{2000}, \delta_{2000}$) for energies 0.5–2 keV for the observations of PSR B0823+26 on 2017 April 22, 24 and 26 (top to bottom, *XMM-Newton* revolutions 3181, 3182, 3183, respectively). The white circles with radii 15 arcsec are centred on the radio position of PSR B0823+26. On April 22 and 26 when the pulsar is in the radio B mode, PSR B0823+26 is evidently present. On the contrary, on April 24 PSR B0823+26 is in the radio Q mode and is not visible in the X-ray map for a similar exposure. The orientation is: North is up and East is left.

collected in the corresponding ~ 1 -hour time interval and applying the ML analysis gives a 4.6σ source detection. Apparently, the 3σ detection in the total observation of April 24 was due to PSR B0823+26 being active in this 1-hour interval. The upper gray horizontal band shows the average count rate during all observations with PSR B0823+26 in the B-mode $(10.81 \pm 0.44) \times 10^{-3}$ cts/s. The lower horizontal band shows for the Q-mode observation of April 24 the average count rate during that observation but excluding the 1-hour interval in which PSR B0823+26 was active $(0.38 \pm 0.42) \times 10^{-3}$ cts/s, consistent with no detection or 2σ upper limit of 1.22×10^{-3} cts/s.

It is interesting to note in Fig. 4 that the count rate (0.2 – 2 keV) over the five days of our campaign with PSR B0823+26 in the B mode does not seem to be constant. The average count rate

Table 3. Jodrell Bank ephemeris of PSR B0823+26 valid for our *XMM-Newton* observations.

Right Ascension (J2000)	$08^{\text{h}}26^{\text{m}}51^{\text{s}}.538$
Declination (J2000)	$+26^{\circ}37'21''.35$
Epoch (TDB)	57579
ν (Hz)	1.8844381708762
$\dot{\nu}$ (Hz s^{-1})	-5.96902×10^{-15}
$\ddot{\nu}$ (Hz s^{-2})	-1.95×10^{-24}
Start (MJD)	57306
End (MJD)	57851
Solar system ephemeris	DE405

measured during the first observation on April 20, $(13.0 \pm 1.0) \times 10^{-3}$ cts/s, is higher by $\sim 3.0\sigma$ than that during the last day on April 30, $(9.0 \pm 0.9) \times 10^{-3}$ cts/s. If we approximate the evolution of the count rate by a linear decay, the best fit gives an improvement by 3.1σ compared to a constant count rate. It is, however, more likely that PSR B0823+26 exhibits, during its radio B mode, some variability in its X-ray flux of order $\pm 20\%$ on time-scales of hours or days.

In Fig. 5 we reproduce the light curve for the Q-mode observation on April 24, 2017, with shorter time intervals of 21 minutes when our counting statistics allowed this. PSR B0823+26 exhibited a radio null mode at the start of the observation until the onset of the short 6–7 minutes Q-bright mode (vertical gray band in Fig. 5), followed by the Q mode for the remaining ~ 4.5 hours. In this figure we selected the shorter time intervals starting at the onset of the radio Q-bright mode. In the first of the short 21-minute intervals (MJD 57867.38) we detected PSR B0823+26 in the X-ray sky map at a significance level of 4.5σ . We did not detect PSR B0823+26 in X-rays during the preceding radio null mode, thus after the onset of the short radio Q-bright mode we measured significant correlated flaring in X-rays with a possible decay over ~ 1.5 hour to measured count rates consistent with zero.

In the Introduction we noted that Becker et al. (2004) detected PSR B0823+26, but with an X-ray count rate that appears now to be significantly lower than the count rate we measure in the radio B mode, and somewhat higher than we measure in the Q mode. To investigate any (in)consistency, we revisited the archival *XMM-Newton* observation of April 26, 2002, and produced the light curve shown in Fig. 6. For easy comparison, we show the average count rates of the B and Q modes as measured in our campaign and drawn in Fig. 4. From this comparison, we conclude that PSR B0823+26 was in the radio B mode at the start of the observation in April 2002 with the same count rate as measured on average in the B mode during our campaign. During the remainder of the 2002 observation, the measured count rates are similar to the values we measured in 2017 April 24 in the Q mode during the decay after the high count rate in the Q-bright mode (see Fig. 5), but most individual values do not represent significant detections.

5 X-RAY TIMING ANALYSIS

For the timing analysis we could only use the Pn data, which had a sufficiently good time resolution of 47.7 ms, and selected events detected within a $20''$ aperture around the X-ray position of PSR B0823+26. The times of arrival were converted to arrival times at the Solar System Barycentre and folded with the ephemeris

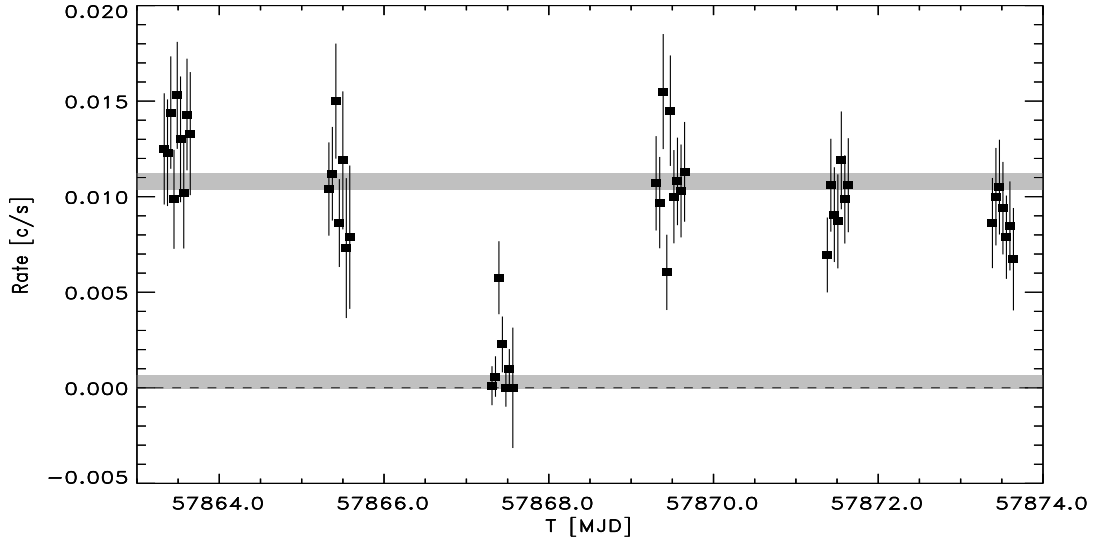


Figure 4. PSR B0823+26 count rates (0.2–2 keV) in time intervals of ~ 1 hour as a function of Modified Julian Day for all our *XMM-Newton* EPIC Pn observations from 2017 April 20 to April 30. Error bars are $\pm 1\sigma$. The upper gray band shows the average count rate during the B-mode observations, $(10.81 \pm 0.44) \times 10^{-3}$ counts s^{-1} , and the lower band the average count rate $(0.38 \pm 0.42) \times 10^{-3}$ counts s^{-1} , thus consistent with no detection) during the Q-mode observation on April 24 excluding the only 1-hour interval in which PSR B0823+26 was significantly (4.6σ) detected. The band widths correspond to 2σ .

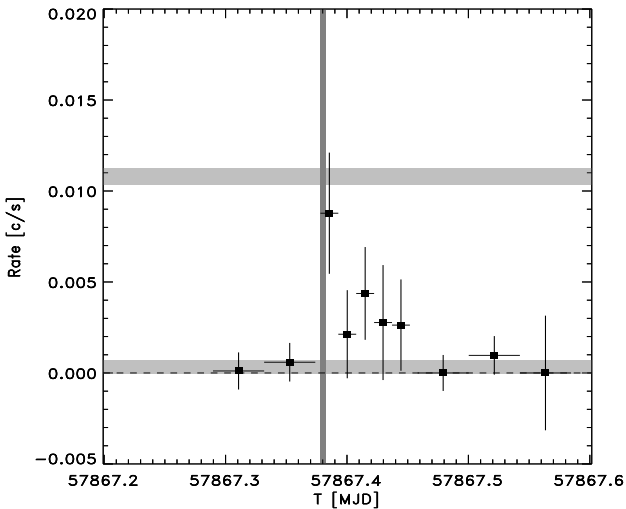


Figure 5. PSR B0823+26 count rates (0.2–2 keV; EPIC Pn) for our observation of 2017 April 24, when PSR B0823+26 was predominantly in the radio Q mode. The first two X-ray values are measured during the initial radio null mode (no significant detection radio and X-ray emission), followed by a short 6–7 minutes interval with enhanced radio emission (Q-bright mode, see Fig. 2), before PSR B0823+26 entered into the Q mode. The vertical gray band indicates the onset and six minutes of the Q-bright mode. The five time bins starting at the onset of the Q-bright mode are 21 minutes wide. The other time bins are 1-hour wide. Error bars are $\pm 1\sigma$. For the horizontal grey bands, see Fig. 4.

of PSR B0823+26 given in Table 3. We searched for a timing signature first in the individual observations, and discovered already in the first observation on April 20, 2017, pulsed X-ray emission from PSR B0823+26 with the detection of a broad pulse in the energy band 0.2–2 keV at a significance of 9.2σ (Z_1^2 value, [Bucccheri et al. 1983](#)). The pulsed signal was detected in all five B-mode observa-

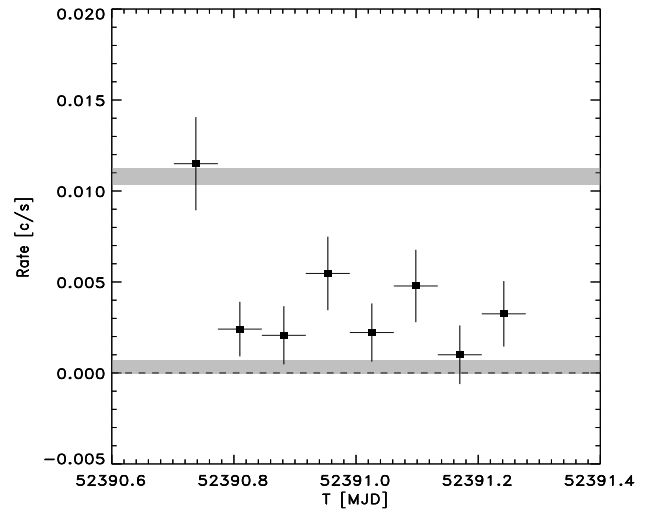


Figure 6. PSR B0823+26 Pn count rates (0.2–2 keV) for the archival observation of 2002 April 26 ([Becker et al. 2004](#)). Error bars are $\pm 1\sigma$. The gray bands are the same as in Fig. 4, and show the average count rates measured during our B-mode observations of 2017 April, and during our Q-mode observation on 2017 April 24, respectively. The band widths correspond to 2σ .

tions, but not in the Q-mode observation on April 24, 2017. The latter is unsurprising, given that no point source was found in the sky map of the Q-mode observation at the position of PSR B0823+26. The 2σ flux upper limit for the energy band 0.5–2 keV, derived in the spatial analysis for the Q mode data (excluding the bright-Q phase), amounts 1.48×10^{-15} erg cm^{-2} s^{-1} , assuming a double-BB spectral shape as used for the B-mode (see Subsection 6.1).

For the sum of all B-mode observations, Fig. 7 shows the X-ray pulse profile of PSR B0823+26 in the 0.2–2 keV energy inter-

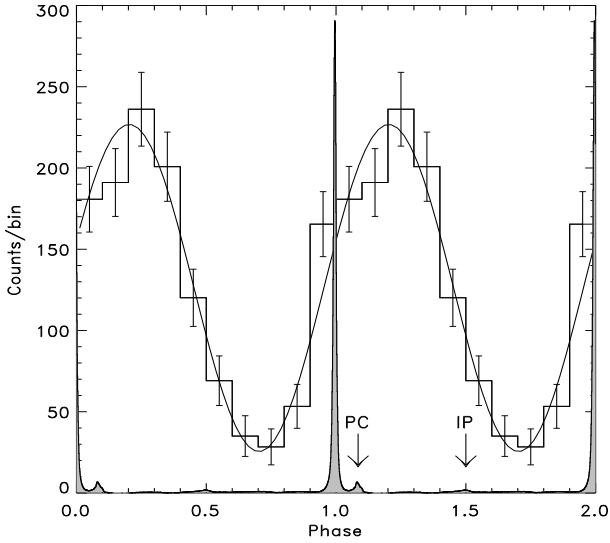


Figure 7. X-ray pulse profile of PSR B0823+26 (histogram) using *XMM-Newton* Pn data for all five B-mode observations for the energy interval 0.2–2 keV, derived by phase-resolved imaging. The celestial background, assumed to be flat, is modelled out. The y-axis gives in 10 phase bins the derived number of pulsed plus unpulsed counts from the point source. Error bars are $\pm 1\sigma$. The solid-line profile shows a fit with a sinusoid peaking at phase 0.203 ± 0.012 . For comparison, the radio profile, as measured with the GMRT at 325 MHz, is also shown. The strong radio main pulse peaks at phase -0.005 and the phases of the much weaker Post Cursor (PC) and Inter pulse (IP) are indicated.

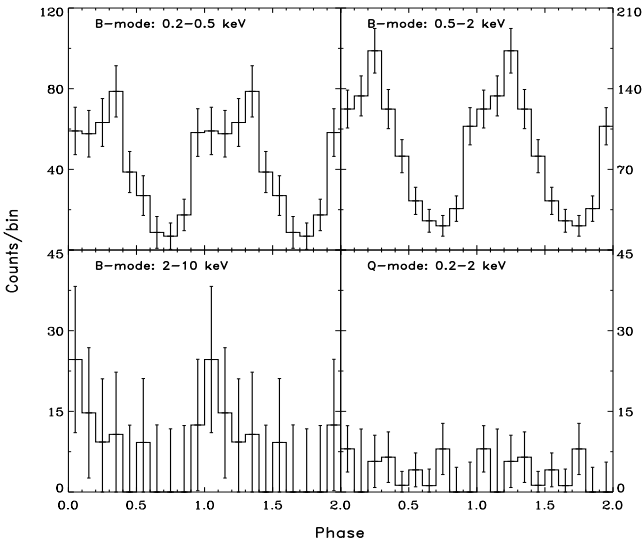


Figure 8. Pulse-phase distributions of PSR B0823+26 like in Fig. 7 combining all five B-mode observations in differential energy intervals between 0.2 and 10 keV, and for the single Q-mode observation of April 24 for energies 0.2–2 keV. A strong broad pulse is detected in the B mode between 0.2 and 2 keV, but no pulsation is found in the Q mode. Error bars are $\pm 1\sigma$.

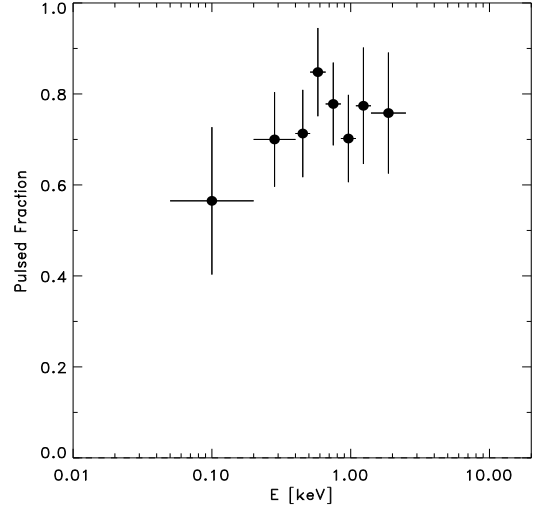


Figure 9. PSR B0823+26 pulsed fraction as a function of energy as derived from a three-dimensional ML analysis (see text). Error bars are $\pm 1\sigma$.

val. This pulse-phase distribution is generated by applying phase-resolved spatial analysis: for each phase bin count sky maps are produced and with the two-dimensional ML method the number of point-source counts is determined per phase bin (Hermesen et al. 2017). In this approach, the sky background has been suppressed, and the phase distribution contains only source counts (pulsed plus unpulsed). The measured profile can be well fitted with a sinusoid and reaches its maximum at phase 0.203 ± 0.012 . The radio profile, as we measured it with the GMRT at 325 MHz, with the strong main pulse at phase -0.005 and the much weaker Post Cursor (PC) and Inter pulse (IP), is also indicated in Fig. 7. The X-ray pulse lags the radio main pulse by 0.208 ± 0.012 in phase.

Fig. 8 shows pulse profiles of PSR B0823+26 in three different energy intervals between 0.2 and 10 keV, and the phase distribution for the Q-mode for energies 0.2–2 keV. Fig. 8 clearly shows for the B mode the detection of the broad X-ray pulse for energies up to 2 keV, and no detection above 2 keV. In the Q mode (total observation on April 24) there is, also in this representation, no indication for an X-ray pulse. The number of source counts detected in the Q-bright interval is too low to construct a pulse profile.

From Fig. 7 it is evident that the measured X-ray pulsed fraction for energies 0.2–2 keV is very high. To derive the pulsed fraction as a function of energy, we applied a three-dimensional ML method: assuming that the pulse profile is sinusoidal across the *XMM-Newton* energy band, we can generalize the two-dimensional ML method by also taking into account the pulse-phase information of the events in a three-dimensional approach (see for details Hermesen et al. (2017)). The derived pulsed fraction as a function of energy is shown in Fig. 9. The values between 0.2 and 2 keV vary over the range ~ 70 to 80%.

6 X-RAY SPECTRAL ANALYSIS

We excluded from all our spectral analyses the observation on April 24, 2017, when the pulsar was successively in the Null, Q-bright and Q mode, and was not detected in the X-ray skymap of the total observation. The X-ray detection in the short Q-bright mode had too few source counts to derive a spectrum as well. Thus, we concentrate on the B mode.

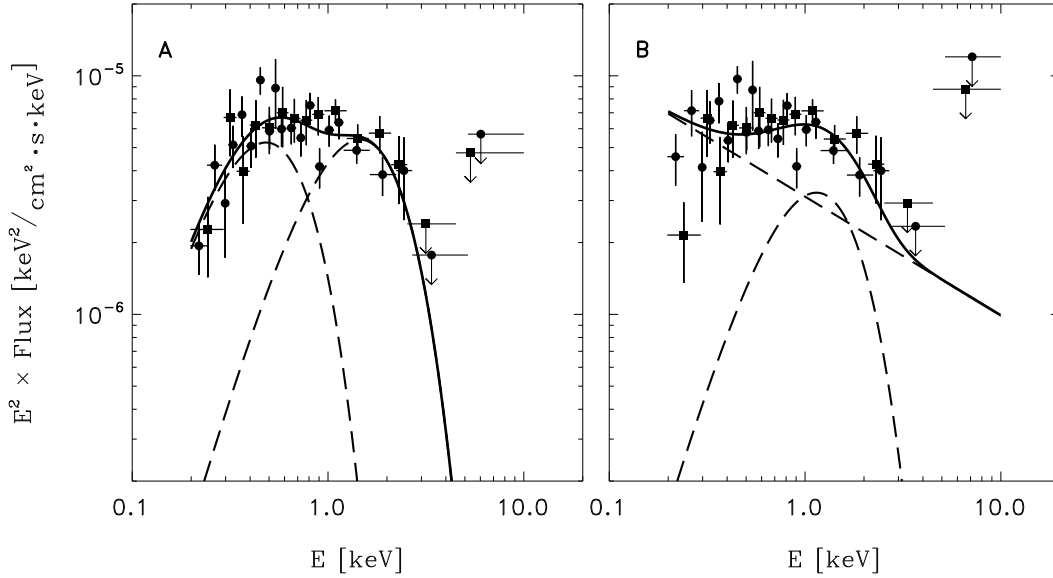


Figure 10. Unabsorbed X-ray photon spectrum of the total emission of PSR B0823+26 in the radio B mode, derived from spatial analysis for *XMM-Newton* EPIC Pn (filled circles) and MOS 1 and 2 (filled squares). *Panel A:* The solid line shows the best fit with two blackbody components ($\sim 30\%$ goodness-of-fit probability); the broken lines show the contribution from a soft ($kT = 0.12$ keV) and a hard component ($kT = 0.37$ keV), respectively. *Panel B:* Similarly, best fit ($\sim 10\%$ probability) with a blackbody ($kT=0.29$ keV) and a power law (index= -2.5). Error bars are $\pm 1\sigma$.

6.1 Spectrum total emission of PSR B0823+26

We first derived the spectral parameters for the total emission from PSR B0823+26 between 0.2 and 10 keV using all the observations in Table 2 during which PSR B0823+26 was in the B mode. We used the Pn and MOS 1 and 2 data and performed again the two-dimensional ML analysis on the counts sky maps for user-defined energy windows between 0.2 and 10 keV, again adopting $\xi = [0, 4]$ and $F = 0$ (see footnote in Section 4). EPIC Pn and MOS 1 and 2 data were treated separately. We fixed the absorbing column density, N_{H} , towards PSR B0823+26 in all our spectral modelling to $3.43 \times 10^{20} \text{cm}^{-2}$ (Kalberla et al. 2005; Dickey & Lockman 1990).

We first produced fits to the total source-count spectrum with a single power law (PL; αE^{Γ} , with α the normalisation and Γ de index) and a single blackbody (BB). Both fits are not acceptable with $\chi_r^2 = 1.91$ (for 38 degrees of freedom (dof)) and $\chi_r^2 = 2.97$ (for 38 dof), respectively. A fit with two blackbodies gave an excellent fit with $\chi_r^2 = 1.12$ (for 36 dof): in this, we use a cooler blackbody with $kT \sim 0.12$ keV with hot spot radius R of ~ 77 m, and a hotter blackbody with $kT \sim 0.37$ keV with R only ~ 8.5 m (see Table 4a and Fig. 10a). However, a fit with a BB plus PL also gave a good fit with $\chi_r^2 = 1.29$ (for 36 dof): $kT \sim 0.29$ keV with $R \sim 11$ m and $\Gamma \sim -2.50$ (see Table 4b and Fig. 10b). The double-BB fit is preferred over the BB-plus-PL fit (goodness of fit probability $\sim 30\%$ versus $\sim 10\%$).

For estimating the spectral shape of the total spectrum, we could use our maximal statistics by using the events detected by the Pn and MOS 1 plus 2. For the spectra of components of the pulsar-phase distribution, we need the timing information and can only use the Pn events. In order to see whether there are systematic differences between the derived parameters for fits to the total spectrum of PSR B0823+26 using Pn and MOS 1 plus 2 data compared to using just Pn data, we repeated the double-BB and BB-plus-PL fits for the latter case. Table 4 shows that we get “identical” fit parameters, and that again the double-BB fit ($\sim 5\%$ probability) is

preferred over the BB-plus-PL fit ($\sim 1\%$ probability). In conclusion, we do not see a systematic difference in the fit results, but mainly a loss in counting statistics when only the Pn data is used.

6.2 Spectra of the pulsed and unpulsed emissions of PSR B0823+26

In Hermsen et al. (2017) we introduced the three-dimensional ML approach. In this approach the ML analysis is applied in the 3D data space where the axes are the two sky coordinates and pulsar rotational phase. The spatial PSF is the point source signature in the skymaps for differential energy intervals and e.g. a sinusoid the shape of the pulse profile in all differential energy bins.

However, in our spectral analysis we consider two possible interpretations/descriptions of the pulse-phase distribution, namely, the measured X-ray pulse profile (e.g. Fig. 7) consists of two components: 1) a flat unpulsed component at the level of the minimum in the profile (DC component), plus a sinusoidal pulse on top of the flat background level (Excess) at the phase of the X-ray Main pulse (ME); 2) two sinusoidal pulses, one at the position of the phase of the X-ray Main pulse (M), and one at the phase of the minimum of the pulse profile, which we call the X-ray Interpulse (IP). The complementary DC and ME (case 1), or M and IP (case 2), source counts per differential energy interval are simultaneously determined in the three-dimensional ML approach, and in the next step converted to source flux values in the forward-folding spectral-fitting procedure.

We first fitted for case 1, the combination of unpulsed emission DC with pulsed excess emission ME. The best fit assigns $\sim 20\%$ of the counts detected from PSR B0823+26 in the Pn data between 0.2 and 10 keV to the DC component and $\sim 80\%$ to the ME pulsed emission. Both component spectra can be perfectly fitted with a single PL model with index $\Gamma = -2.2$. However, this is inconsistent with the spectrum of the total emission. Namely, the pulsed fraction is close to 80%, and we found that the total spec-

Table 4. Spectral fits to the total emission spectrum and to the pulsed and unpulsed (DC) emissions of PSR B0823+26 in the B mode over the energy range 0.2-10 keV using MOS 1&2 and/or Pn data of all XMM-Newton observations of the 2017 campaign. For the pulsed emission, two cases are considered: 1) the pulsed counts are defined as the excess counts in the main X-ray pulse above a flat background level, *Pulse-ME*; 2) it is assumed that there are two sinusoidal pulses in the light curve, namely one strong pulse at the main X-ray pulse, *Pulse-M*, and one corresponding to an antipodal inter pulse, *Pulse-IP*. Table **I**), fits with two black-body models (BB); Table **II**), fits with a power-law (PL) and black-body (BB) model. N_H has been kept fixed at a value of $3.43 \times 10^{20} \text{ cm}^{-2}$. Values for kT in bold are kept fixed (see text).

Model	Total	Total	Pulsed	DC	Pulsed	Pulsed
Fit par.	Pn/MOS1+2	Pn	<i>Pulse-ME</i>		<i>Pulse-M</i>	<i>Pulse-IP</i>
I						
	BB+BB	BB+BB	BB+BB	BB+BB	BB+BB	BB+BB
$\alpha_{BB1} \times 10^2$	0.48 ± 0.17	0.60 ± 0.27	0.31 ± 0.19	0.14 ± 0.05	$0.39^{+0.43}_{-0.20}$	0.07 ± 0.02
kT_1	0.12 ± 0.01	0.12 ± 0.01	0.13 ± 0.03	0.12	0.13 ± 0.02	0.12
R_{BB1}	77 ± 14	86 ± 20	62 ± 19	41.5 ± 7.4	70^{+38}_{-18}	29.4 ± 4.2
$F_{BB1} \times 10^{15}$	4.5 ± 0.5	4.2 ± 0.5	4.4 ± 0.7	1.1 ± 0.4	4.8 ± 0.8	0.6 ± 0.2
$\alpha_{BB2} \times 10^5$	5.90 ± 2.25	6.54 ± 3.50	2.55 ± 3.40	1.3 ± 0.5	$3.0^{+4.22}_{-1.81}$	0.65 ± 0.25
kT_2	0.37 ± 0.03	0.36 ± 0.04	0.41 ± 0.13	0.37	$0.41^{+0.13}_{-0.09}$	0.37
R_{BB2}	8.5 ± 1.6	8.9 ± 2.4	5.6 ± 3.9	4.0 ± 0.8	$6.1^{+4.3}_{-1.8}$	2.8 ± 0.5
$F_{BB2} \times 10^{15}$	$8.5^{+0.8}_{-0.9}$	8.0 ± 1.0	4.9 ± 1.2	1.8 ± 0.7	5.9 ± 1.4	0.92 ± 0.35
χ_r^2 / dof	1.12 / 36	1.60 / 17	0.30 / 4	0.54/6	0.34 / 4	0.54/6
II						
	BB+PL	BB+PL	BB+PL	BB+PL	BB+PL	BB+PL
$\alpha_{BB} \times 10^3$	0.09 ± 0.04	0.13 ± 0.09	0.4 ± 0.7	0.014 ± 0.012	0.4 ± 0.8	0.007 ± 0.006
kT	0.29 ± 0.03	0.25 ± 0.05	0.18 ± 0.05	0.29	0.18 ± 0.06	0.29
R_{BB}	11 ± 3	13 ± 5	23 ± 20	4.2 ± 1.8	23 ± 23	2.9 ± 1.2
$F_{BB} \times 10^{15}$	5.1 ± 0.9	3.6 ± 1.0	3.0 ± 1.0	0.8 ± 0.7	2.8 ± 1.1	0.4 ± 0.3
$\alpha_{Pl} \times 10^6$	3.12 ± 0.51	3.44 ± 0.67	2.66 ± 0.75	0.9 ± 0.2	3.38 ± 0.84	0.5 ± 0.1
Γ	-2.50 ± 0.17	-2.39 ± 0.20	-2.13 ± 0.36	-2.50	-2.15 ± 0.33	-2.50
$F_{Pl} \times 10^{15}$	7.5 ± 0.7	8.2 ± 0.8	5.8 ± 1.0	2.0 ± 0.5	7.4 ± 1.2	1.0 ± 0.3
χ_r^2 / dof	1.29 / 36	1.92 / 17	1.14 / 4	0.26/6	0.85 / 4	0.26/6

Units: N_H in cm^{-2} ; α_{BB} in $\text{photons cm}^{-2} \text{ s}^{-1} \text{ keV}^{-3}$; kT in keV; Fluxes F are unabsorbed for the 0.5-2 keV band in $\text{erg}/(\text{cm}^2 \text{ s})$; Hot spot radius R_{BB} in meters adopting a source distance of 357 pc; α_{Pl} in $\text{photons cm}^{-2} \text{ s}^{-1} \text{ keV}^{-1}$ at 1 keV

trum can not be explained with a single PL model, but that two components are required. Indeed, we can also obtain an excellent fit with a double-BB model (see Table 4a) and with a BB-plus-PL model (see Table 4b) to the pulsed emission ME. The obtained temperatures and PL index are fully consistent with those derived for the total emission spectrum using our maximal statistics with Pn and MOS 1 plus 2 data. However, the number of free parameters went down from 36 to only 4, reflecting the loss in statistical accuracy due to the lower number of counts and energy bins available in the three-dimensional ML analysis. A spectral fit with two components to the very-low-statistics DC spectrum does not converge and we need to reduce the number of free parameters. For comparison purposes, we fixed the two BB temperatures, or the temperature of a BB and the spectral index of a PL component, in fits to the DC spectrum to the values obtained for the total emission (see Table 4).

For case 2, fitting the spectra of an X-ray Main pulse (M) and an Interpulse (IP), together producing the measured pulse-phase distribution, we followed the same procedure as for case 1, with very similar results (see Tables 4). This is no surprise, because, by definition, the total counts assigned to M are $\sim 12.5\%$ higher than for ME, and the number of counts assigned to IP are $\sim 50\%$ of the counts assigned to DC.

In general, the fits with two blackbodies (to the total spectra and the pulsed spectra) are better than with a BB plus PL. Also, the two temperatures and the radii of the hot spots derived in the fits to the total and pulsed spectra are consistent, within 1σ . We conclude that the total spectrum and the pulsed emission are most likely the

sum of two blackbodies, but an interpretation with a BB plus PL can not be excluded.

6.3 Magnetized-atmosphere-model spectral fit to the total emission spectrum of PSR B0823+26

While the spectrum of PSR B0823+26 can be well-fit by the sum of two blackbody spectra (see Subsection 6.2), it is more physically correct to describe thermal emission from the surface of a hot neutron star by an atmosphere model. Spectral fits using atmosphere models generally yield lower temperature and larger emission radius than fits obtained using blackbodies (Romani 1987; Shibano et al. 1992). Furthermore, emission is anisotropic, with a beam pattern (i.e. specific intensity as a function of photon propagation angle) that is energy-dependent, especially when the atmospheric plasma is strongly magnetized, as in the case of PSR B0823+26 with an inferred (equatorial) magnetic field of $\sim 10^{12}$ G (see Section 1). This last point makes it possible to achieve very high pulsed fractions, as we measured for PSR B0823+26. Therefore we employ a magnetized partially ionized hydrogen atmosphere model (Ho et al. 2008; Ho 2014) to generate X-ray spectra and pulse profiles with a procedure that accounts for relativistic effects (Ho 2007). We consider a magnetic field of 10^{12} G that is directed parallel to the surface normal; field strengths of 5×10^{11} and 2×10^{12} G do not change our results qualitatively. We assume a neutron star mass M of $1.6M_\odot$ and radius of 10 km, so that the gravitational redshift is $1 + z = 1.38$. We denote by α the angle

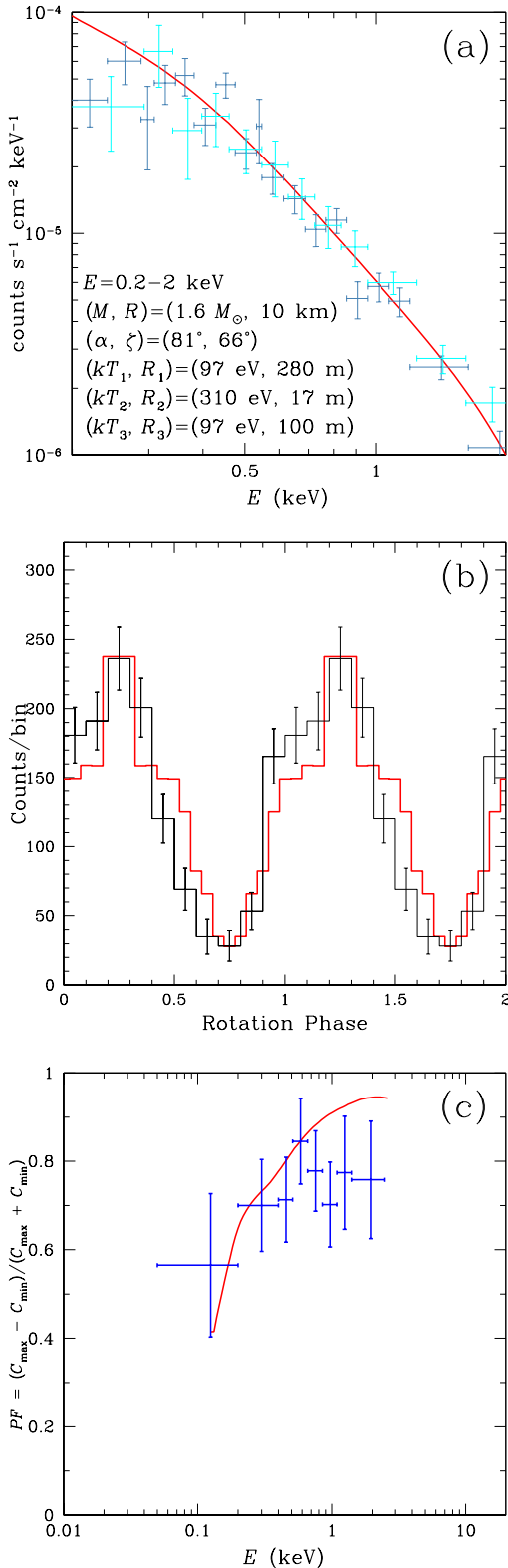


Figure 11. PSR B0823+26 in the radio B mode. a), unabsorbed X-ray photon spectrum of the total emission for *XMM-Newton* EPIC Pn (dark blue) and MOS 1 and 2 (light blue); b), pulse profile for 0.2 – 2 keV; c), pulsed fraction PF . The red curves show the best fit with a (redshifted) magnetized partially ionized hydrogen atmosphere model. For best fit parameters: see text and parameters in figure a). The definition of PF in the model calculations (with C_{max} and C_{min} the maximum and minimum counts, respectively), is for a sinusoidal pulse consistent with the definition used in the analysis. The model profile in figure b is approximately aligned with the observed one. Error bars are $\pm 1\sigma$.

between the magnetic and rotation axes and by ζ the angle between the rotation axis and the line of sight, and we note that (α, ζ) and (ζ, α) yield the same X-ray spectrum and pulse profile. For PSR B0823+26, fits to radio polarization data using the rotating vector model give $(\alpha, \zeta) = (81^\circ, 84^\circ)$, with an uncertainty of 0.7° , for antipodal hot spots (Everett & Weisberg 2001). However, models with these angles produce X-ray pulse profiles that have a peak which is too narrow to match that obtained from *XMM-Newton* data (see Figure 7) because this geometry only permits the narrow component (of width < 0.1 in rotation phase; Pavlov et al. 1994) of the beam pattern to be visible. Thus, while we assume $\alpha = 81^\circ$, we allow ζ to vary.

We are able to approximately match the X-ray spectrum, pulse profile, and pulsed fraction of PSR B0823+26 with a model that includes three emission components: a primary spot with a small hot core ($kT_2 = 310$ eV, $R_2 = 17$ m) and a larger cooler annular concentric ring ($kT_1 = 97$ eV, $R_1 = 280$ m) and an antipodal hot spot ($kT_3 = 97$ eV, $R_3 = 100$ m) which largely produces the flux at pulse minimum (see Fig. 11). Note that our model fitting of the X-ray characteristics requires a best-fit $\zeta \sim 66^\circ$ in contrast to that found by modelling radio observations ($\zeta \sim 84^\circ$). This discrepancy will be addressed in the Discussion. Interestingly, we verified that adding a hot core to the cooler component in the antipodal spot does not make a noticeable difference to the modelled pulse profile and pulsed fraction. This is because the beam/pulse profile of the extra antipodal hot spot is very narrow, and given the geometry, we are not seeing the hot core of the antipodal cap. In other words, if the two polar caps have the same temperatures (but somewhat different sizes), then this agrees with the X-ray observations.

7 SUMMARY

Our long *XMM-Newton* X-ray and GMRT/LOFAR radio observations of PSR B0823+26 revealed, after PSR B0943+10, a second example of simultaneous X-ray/radio moding, and we could study its X-ray characteristics in great detail. First, we will present a summary of the new findings of our X-ray radio campaign.

(i) We found PSR B0823+26 during five out of our six *XMM-Newton* observations to be in the radio B mode and during only one observation, on April 24, 2017, in the Q mode. Over our entire radio coverage with GMRT and LOFAR of ~ 80 hours, PSR B0823+26 spent only $\sim 15\%$ of the time in Q mode.

(ii) We discovered correlated X-ray/radio moding: during the five X-ray observations with PSR B0823+26 in the radio B mode, the pulsar is detected in the skymaps with an average count rate of $(10.81 \pm 0.44) \times 10^{-3}$ cts/s (0.2–2 keV), and during the single radio Q mode it is not detected down to a 2σ upper limit of 1.22×10^{-3} cts/s.

(iii) A new manifestation of X-ray variability of pulsars was discovered in terms of a variation in the average X-ray flux in the five B-mode observations. The average flux varied by $\pm 20\%$ around the average value.

(iv) In the April-24 observation PSR B0823+26 started in the radio Null mode, then spent 6–7 minutes in the Q-bright mode, and then gradually faded to the Q mode in which it stayed for 7 h and 50 minutes.

(v) The X-ray behaviour was correlated with the successive radio modes during the April-24 observation. During the initial radio Null mode PSR B0823+26 was not detected in X-rays, but during an interval of 21 minutes including the Q-bright mode a strong (4.5σ) detection was made in the spatial analysis which then ap-

peared to decay over ~ 1.5 hours to non-detectable X-ray emission in the remaining 7 hours of the Q mode.

(vi) In the radio B mode, we discovered X-ray pulsations from PSR B0823+26 between 0.2 and 2 keV with a broad sinusoidal pulse. The X-ray pulse significantly lags the radio MP by 0.208 ± 0.012 in phase. There is no pulse visible around the phase of the IP, but a weak sinusoidal X-ray IP can be hidden under the minimum level of the light curve. In the Q mode we found no indication of a pulsed signal in our X-ray data.

(vii) The X-ray pulsed fraction we found to be very high, ~ 70 – 80% for energies between 0.2 and 2 keV.

(viii) The spectrum of the total X-ray emission is well described by a double blackbody model (goodness of fit probability $\sim 30\%$) as well as by a blackbody plus power-law model ($\sim 10\%$ probability). The double-BB model has a cool component with $kT \sim 0.12$ keV ($\sim 1.4 \times 10^6$ K) with hot spot radius of ~ 77 m, and a hotter blackbody with $kT \sim 0.37$ keV ($\sim 4.3 \times 10^6$ K) and radius ~ 8.5 m. For the BB-plus-PL model the parameters were: $kT \sim 0.29$ keV ($\sim 3.4 \times 10^6$ K) with hot spot radius of ~ 11 m, and PL index $\Gamma \sim -2.50$.

(ix) The spectrum of the pulsed emission is also well fit with a double-BB model (goodness of fit probability $\sim 10\%$) with the same parameters as for the total spectrum, and also with a BB-plus-PL model ($\sim 5\%$ probability) with a somewhat lower temperature $kT \sim 0.18$ keV, but the uncertainties on hot spot radius and PL index become large.

(x) The spectrum of a complementary unpulsed emission, or of an Interpulse, is not well constraint due to the low counting statistics available.

(xi) Alternatively, the total spectrum of PSR B0823+26, its pulse profile and pulsed fraction as a function of energy can all be reproduced with a magnetized partially ionized hydrogen atmosphere model with three emission components, a primary spot with a small hot core ($kT_2 \sim 310$ eV or $\sim 3.6 \times 10^6$ K, $R_2 \sim 17$ m) and a larger cooler concentric ring ($kT_1 \sim 97$ eV or $\sim 1.1 \times 10^6$ K, $R_2 \sim 280$ m) and an antipodal hot spot ($kT_3 \sim 97$ eV, $R_3 \sim 100$ m). However, this atmosphere-model fit to our X-ray data requires the angle ζ between the rotation axis and line of sight direction to be $\sim 66^\circ$, in conflict with the accurately radio-derived value of $\sim 84^\circ$.

(xii) Adding in the atmosphere-model fit a fourth emission component, namely a hot core in the antipodal cap such that the two polar caps have the same temperatures (but somewhat different sizes), would also be in agreement with the X-ray observations.

8 DISCUSSION

8.1 X-ray moding: PSRs B0943+10, B1822–09 and B0823+26

To date, long simultaneous X-ray/radio campaigns on radio-mode-switching pulsars have only been performed on PSR B0943+10 (Hermesen et al. 2013; Mereghetti et al. 2016), PSR B1822–09 (Hermesen et al. 2017) and on PSR B0823+26, presented in this work. The discovery of synchronous X-ray/radio mode switching was reported for the nearly aligned PSR B0943+10: its X-ray flux switched in *anti correlation* with the radio flux: when the pulsar is in a radio “bright” (B) mode the X-ray flux is weak, and when it switches to a radio “quiet” (Q) mode, the X-ray flux more than doubles (Hermesen et al. 2013). In both radio modes the X-ray emission is the sum of a pulsed thermal component with

$T_h \sim 3.4 \times 10^6$ K (hot spot radius $R_h \sim 21$ m) plus an about equally strong unpulsed non-thermal component with photon index ~ -2.5 (Mereghetti et al. 2016). However, for the nearly orthogonal PSR B1822–09 no indication was found for synchronous X-ray/radio moding and its total X-ray spectrum could be fitted with two black bodies, a cool component ($T_c \sim 1.0 \times 10^6$ K, $R_c \sim 2.0$ km) and a hot component ($T_h \sim 2.2 \times 10^6$ K, $R_h \sim 100$ m) (Hermesen et al. 2017). In this work on the nearly orthogonal PSR B0823+26, we report the discovery of a second example of synchronous X-ray/radio mode switching.

Most surprisingly, the characteristics of the X-ray moding and X-ray emission of PSR B0823+26 are very different from those reported for PSR B0943+10. In particular, we revealed *correlated* X-ray/radio moding: in the radio B mode PSR B0823+26 is detected in X-rays and exhibits a dominant pulsed component, while the pulsar is not detected during the radio Q mode, with a 2σ flux upper limit a factor ~ 9 below the X-ray flux in the B mode. We showed that the total emission of PSR B0823+26 can also be described by a black-body and power-law component with the same temperature and index as measured for PSR B0943+10. The difference being that for PSR B0823+26 both components contribute to the pulsed emission, while the pulsed emission of PSR B0943+10 is purely thermal. However, the statistically preferred model spectrum for PSR B0823+26 consists of two black bodies, a hot (small hot spot radius $R_h \sim 8.5$ m) component with $T_h \sim 4.3 \times 10^6$ K and a cool (broader R_c of ~ 77 m) component with $T_c \sim 1.4 \times 10^6$ K. In our discussion we will address this latter preferred spectral shape.

The aim of our campaign was to further our understanding of X-ray/radio mode switching. However, the emerging picture is becoming increasingly more complex. The three pulsars have different geometries (orientations of magnetic and rotation axes and viewing angles), different X-ray spectral shapes and/or different mode-switching characteristics (mode durations and correlated/anti correlated or no X-ray/radio mode switching). On the other hand, for all three pulsars we detected broad sinusoidal X-ray pulse profiles with (very) high pulsed fractions between $\sim 60\%$ and $\sim 80\%$ around 1 keV. Table 5 summarises the radio and X-ray characteristics. In the discussion we will address the different moding characteristics, the differences in X-ray spectral and timing properties, as well as the enigmatic problem of what might cause mode switching in pulsars.

8.2 X-ray mode-switch time scales

PSR B0943+10 and PSR B0823+26 are both old pulsars ($\tau \sim 5$ Myr) and exhibit mode durations of the order of hours, while the much younger PSR B1822–09 ($\tau \sim 0.2$ Myr) switches radio modes on time scales of minutes. Within the uncertainties of radio single-pulse studies, radio-mode switches are seen to occur on time scales of single rotations. In our X-ray data we can not accurately study mode-switch time scales, because these pulsars are weak X-ray sources from which we measure with *XMM-Newton* count rates of order 0.01 cts s^{-1} . An attempt was made for PSR B0943+10: the X-ray mode transitions were studied in X-ray light curves obtained by *stacking* all the Q to B and B to Q mode transitions observed in a campaign in 2014 (Fig. 6 in Mereghetti et al. (2016)). Within the available statistics it was concluded that the X-ray transition occurred within 15 minutes after the radio switch. In Fig. 5, we show for a *single* transition of PSR B0823+26 that the X-ray emission was significantly detected in a time interval of 21 minutes after the switch from a null mode to the short radio Q-bright mode

Table 5. Comparison of radio and X-ray characteristics of the only mode-switching pulsars that are so far observed simultaneously in the radio and X-ray bands. The errors on the parameters derived in the X-ray analyses are for PSR B0823+26 given in the previous sections, and for PSR B0943+10 and PSR B1822–09 by [Mereghetti et al. \(2016\)](#) and [Hermsen et al. \(2017\)](#), respectively.

	PSR B0823+26	PSR B0943+10	PSR B1822–09
P [s]	0.53	1.1	0.77
\dot{P} [s s^{-1}]	1.7×10^{-15}	3.5×10^{-15}	5.3×10^{-14}
τ [Myr]	5	5	0.2
B [G]	9.6×10^{11}	4×10^{12}	6.5×10^{12}
\dot{E}_{rot} [erg s^{-1}]	4.5×10^{32}	10^{32}	4.6×10^{33}
Distance [pc]	320 ⁱ	630 ⁱⁱ	900 ⁱⁱⁱ
Geometry	nearly orthogonal	nearly aligned	nearly orthogonal
Radio-mode duration	~hours	~ hours	~minutes
Radio X-ray moding	correlated	anti correlated	none
X-ray pulse profile	sinusoidal	sinusoidal	sinusoidal
X-ray pulsed fraction*	B: ~80%	B: ~35%	~15% – ~60%
	Q: no detection	Q: ~20% – ~65%	
Total X-ray spectrum	BB ₁ +BB ₂ **	BB ₁ +PL (index -2.5)	BB ₁ +BB ₂
T_{BB_1} [K]	1.4×10^6	3.0×10^6	1.0×10^6
R_{BB_1} [m]	77	21	2000
T_{BB_2} [K]	4.3×10^6		2.2×10^6
R_{BB_2} [m]	8.5		100
L_X Total [erg s^{-1}]	1.6×10^{29}		3.7×10^{30}
L_X B mode [erg s^{-1}]		BB: 1.9×10^{29} PL: 0.8×10^{29}	
L_X Q mode [erg s^{-1}]		BB: 2.3×10^{29} PL: 3.5×10^{29}	
Pulsed X-ray spectrum***	BB+BB**	BB	BB+BB
L_X Pulsed Total [erg s^{-1}]			1.0×10^{30}
L_X Pulsed B mode [erg s^{-1}]	1.1×10^{29}	1.0×10^{29}	
L_X Pulsed Q mode [erg s^{-1}]		2.9×10^{29}	

ⁱ [Verbiest et al. \(2012\)](#); ⁱⁱ based on a pulsar dispersion measure of 15.32 pc cm^{-3} ([Bilous et al. 2016](#)) and the [Cordes & Lazio \(2002\)](#) galactic electron density distribution;

a more recent electron density model ([Yao et al. 2017](#)) gives a larger distance of 890 pc;

ⁱⁱⁱ [Zou et al. \(2005\)](#); an upper limit to the distance of 1.9 kpc is given by [Verbiest et al. \(2012\)](#).

*Average value over energy interval 0.2 – 2 keV or values at start and end of this energy interval;

**Less likely fit with BB ($T = 3.0 \times 10^6 \text{ K}$) + PL (index -2.5).

***For definition pulsed emission see Table 4: *Pulse-ME*. All luminosities L_X for energies 0.5–2 keV.

on 24 April. The low *XMM-Newton* counting statistics of this weak X-ray source do not allow us to study single X-ray mode switches on shorter time scales even though the *XMM-Newton* time resolution is 47.7 ms. Therefore, we can not exclude that the explanation for the non detection of X-ray moding of PSR B1822–09 is that the minutes long mode durations of PSR B1822–09 are too short to allow the pulsar to react in X-rays to a radio-mode switch.

In Fig. 4 we presented the PSR B0823+26 count rates (0.2–2 keV) in time intervals of ~1 hour covering all six observations of our campaign in April 2017. This figure revealed the PSR B0823+26 X-ray variability due to radio-mode switching, but also that the X-ray count rate in the B-mode is not constant. This is a new phenomenon. X-ray emission from radio pulsars was for decades considered to be stable, until the discovery of synchronous X-ray/radio mode switching. Also, two high-B pulsars exhibited magnetar-like outbursts, PSR J1846–0258 ([Gavriil et al. 2008](#)) and PSR J1119–6127 ([Antonopoulou et al. 2016](#); [Archibald et al. 2016](#)), but what we see here is different. There appears to be some variability in the X-ray flux of order $\pm 20\%$ on time scales of hours. E.g. the average X-ray flux during our 9-hours observation on 20 April was ~40% higher than during our 7-hours observation on 30 April.

When we examined our GMRT monitoring data to identify the radio modes, we noticed that in the B mode, the pulsar is bright and displays short (a few pulses) nulls. Also, on 28 April 2017 during the B mode there are short durations of about 200 pulses of weak emission, but different from the Q state, and not classified as a separate mode. If the frequency and lengths of short nulls or the short durations of weak emission during the B mode varies, such as recently discussed for PSR J1822–2256 ([Basu & Mitra 2018](#)), and these occurred e.g. more frequently in our observation on 20 April compared to 30 April, then this might offer an explanation for the variations in average X-ray count rates. However, if that is the explanation, it would also mean that the X-ray flux is closely correlated with the radio flux on time scales of possibly even a few pulses. If that would apply for PSR B1822–09 as well, then mode switching in its X-ray emission could also have been detected for its short mode durations of minutes. A detailed single-pulse study of our radio observations of PSR B0823+26 is required to investigate such a possible tight X-ray/radio correlation, but it is beyond the scope of this work and will be addressed in a follow-up investigation.

8.3 X-ray characteristics: broad thermal pulses, high pulsed fractions from hot polar caps

We noted above that all three pulsars exhibit broad sinusoidal pulse profiles with very high pulsed fractions. PSR B0943+10 has a pulsed fraction in the Q mode that increases with energy from $\sim 20\%$ at 0.2 keV to $\sim 65\%$ at 2 keV, while the X-ray pulsed fraction in the B mode ($\sim 38\%$) did not vary with energy (Mereghetti et al. 2016). For PSR B1822–09 similar pulsed fractions were reported: $\sim 15\%$ around 0.3 keV up to $\sim 60\%$ at 1 keV (Hermsen et al. 2017), and for PSR B0823+26 we find in the B mode even higher pulsed fractions ($\sim 70\text{--}80\%$ for energies 0.2–2 keV). Furthermore, for all three pulsars the pulsed emissions are thermal. Namely, a single black-body spectrum for PSR B0943+10, and double-black-body spectra for PSR B0823+26 and PSR B1822–09. In addition, the derived values for R_{BB} are smaller than the radius of the polar cap, defined by the last closed lines in a dipolar field geometry, $R_{PC} = ((2\pi R^3)/(Pc))^{1/2}$, with the exception of the cool component of PSR B1822–09. For the latter pulsar, which is more than an order of magnitude younger and has a rotational energy loss an order of magnitude larger (see Table 5), $R_{BBc} = \sim 2$ km, compared to a polar-cap radius of 165 m (assuming $R=10$ km). This cooler component might be related to thermal emission from the entire surface.

Thus the hot thermal components of PSR B0943+10, PSR B1822–09 and PSR B0823+26, as well as the cooler component of PSR B0823+26, have R_{BB} smaller than their polar cap radii. These polar hot spots are explained as the result of bombardment of the polar cap by electrons accelerated along the last closed field lines towards the neutron star. However, such high pulsed fractions can not be explained with models in which thermal emission is isotropically emitted from hot polar caps. Including gravitational light bending, it has been shown that the pulsed fraction can not exceed 30% (Pechenick et al. 1983; Beloborodov 2002; Bogdanov et al. 2007; Bogdanov 2016). This is the case for nearly orthogonal geometries (PSR B0823+26 and PSR B1822–09), as well as for nearly aligned pulsars (PSR B0943+10).

In Section 6.3, we showed that a more physically correct atmosphere model can reproduce very high pulsed fractions up to $\sim 90\%$ for pulsars with sufficiently strong magnetic fields. For modelling the case of the nearly orthogonal PSR B0823+26, with both poles visible every rotation, we used a magnetized partially ionized hydrogen atmosphere model and took relativistic effects into account (Ho 2007). The X-ray spectrum, pulse profile and pulsed fractions of PSR B0823+26 were shown to be approximately matched (see Fig. 11) with a model that includes three emission components: a primary spot with a small hot core ($T_{h1} = 3.6 \times 10^6$ K, $R_{h1} = 17$ m) and a larger cooler annular ring ($T_{c1} = 1.1 \times 10^6$ K, $R_{c1} = 280$ m), and an antipodal ‘cool’ spot ($T_{c2} = 1.1 \times 10^6$ K, $R_{c2} = 100$ m). Adding an extra antipodal hot spot in the model does not make a significant difference in the predicted X-ray characteristics, thus, interestingly, if the two polar caps have the same temperatures (but somewhat different measured sizes), this also agrees with the X-ray data. It is interesting to note that the radius for the cool primary component (280 m) is similar to the polar cap radius: R_{PC} is 199 m for $R = 10$ km and 295 m for $R = 13$ km.

PSR B0943+10 is a rotator that is viewed under an angle of only 9° (Deshpande & Rankin 2001). For such a geometry one polar cap is viewed continuously, and one would expect to observe a practically flat pulse-phase distribution if the thermal emission originates in an isotropically emitting hot spot. Storch et al. (2014) showed that also for this geometry of PSR B0943+10 pulsed frac-

tions close to 60% (see also (Mereghetti et al. 2016)) can be explained by including the beaming effects of a magnetised atmosphere, while remaining consistent with the dipole field geometry constrained by radio observations. The latter is, unfortunately, not the case for PSR B0823+26. The successful modelling of the X-ray characteristics of PSR B0823+26 as shown in Fig. 11, was realised for values of $\alpha = 81^\circ$, the angle between the magnetic and rotation axes, and by $\zeta = 66^\circ$, the angle between the rotation axis and the line of sight. An acceptable solution can also be obtained for $(\alpha, \zeta) = (66^\circ, 81^\circ)$. We noted that fits to radio polarisation data using the rotating vector model give $(\alpha, \zeta) = (81^\circ, 84^\circ)$, with an uncertainty of 0.7° (Everett & Weisberg 2001). Therefore, in either case there is an inconsistency between the radio and X-ray derived geometries. Furthermore, the broad X-ray pulse is lagging the radio main pulse in phase by as much as 0.208 ± 0.012 . In order to explain such a large phase shift, one might have to invoke a displaced dipole geometry or a non-dipolar magnetic field close to the surface where the X-rays are produced. Nevertheless, it is not obvious how to relate the phase shift to the different geometrical angles derived from the X-ray and radio characteristics.

In Section 6.1 we concluded that with lower probability (goodness of fit 10%) the X-ray spectrum of PSR B0823+26 can also be described as the sum of a black body ($T \sim 3.4 \times 10^6$ K, $R_{PC} \sim 11$ m) and a power law (index -2.5), with the same spectral parameters as derived for PSR B0943+10. For the latter pulsar, its pulsed emission is thermal (for a possible explanation, see above), and its unpulsed component is non-thermal. For its nearly aligned geometry the unpulsed emission could be non-thermal beamed emission, continuously viewed under the small viewing angle. Could such an explanation also work for the nearly orthogonal PSR B0823+26? In that case the pulsed emission is the sum of a thermal component plus a non-thermal component, *both* contributing to the broad pulse profile. Thus the thermal and non-thermal emissions should both be beamed in the same direction and both beams should be broad. Alternatively, the beams are narrow and shifted in phase by e.g. 0.2, together forming the measured broad profile. In the latter case the shape of the pulse profile should be energy dependent. However, in Fig. 8 the profile shapes in the energy intervals 0.2–0.5 and 0.5–2 keV are statistically identical. Furthermore, for a nearly orthogonal geometry and a viewing angle close to 90° , one would then expect to see beams of non-thermal emission from both poles.

8.4 The nature of mode changing in PSR B0823+26

The results of our campaign are difficult to interpret consistently in terms of current ideas about the nature of polar cap physics and to reconcile the directions of the radio and X-ray emission beaming in PSR B0823+26 (Sections 6.3 and 8.3). It is therefore useful to stand back and ask more fundamental questions about the nature of mode-changing in this pulsar. Our clear result that the pulsed X-rays of PSR B0823+26 switch on and off in tandem with the radio mode switch stands in stark contrast to the result of our earlier campaign on PSR B1822–09 in which no detectable X-ray mode switch was found. Both pulsars are near-perpendicular rotators and exhibit clearly-defined modes designated as B(right) and Q(quiet). So why are they so different?

The most obvious and immediate difference between these pulsars is the timescale and relative intensity of their radio-defined modes. In PSR B1822–09 the separate modes are rarely sustained for an hour and are mostly of far shorter duration, so mode changes occur typically every few minutes (Hermsen et al. 2017). Our sustained observations here have shown that in PSR B0823+26 the

modes appear to be much more stable, with both B and Q lasting many hours, possibly even days. Further, the average intensities of the B/Q modes in PSR B1822–09 is just 2:1 (Fowler et al. 1981), while in PSR B0823+26 Sobey et al. (2015) report that the Q mode is on average a factor ~ 200 dimmer than the B mode, such that earlier workers had assumed the Q mode to be a sustained null (Young et al. 2012).

The character of the modal emission in each pulsar is also very different. In PSR B1822–09 the onset of both the B and Q modes occur within a few pulses, and while there is evidence of occasional complex modal overlap (Latham et al. 2012), there is no suggestion of one mode gradually fading into another. The duration of each mode has a bimodal distribution (Hermsen et al. 2017), the shorter modes being of the order of minutes and the other tens of minutes. Each mode has been found to have a characteristic modulation timescale, which, in shorter mode sequences at least, seems to determine the duration of the mode. A striking feature of the radio observations is that the precursor suddenly becomes present in the B mode and vanishes in the Q mode and coincides with the disappearance of the IP, suggesting a rapid reorganisation of the entire magnetosphere (Goodwin et al. 2004; Contopoulos 2005; Timokhin 2010).

The radio emission of PSR B0823+26 does not show this high degree of organisation. The onset of the B mode after the Q mode is indeed sudden, as in PSR B1822–09 but the transition back to quiescence is better characterised as ‘flickering’: a gradual lessening in the overall brightness of individual pulses and an increase in the number of apparently weak or null pulses. This behaviour is present on a wide range of timescales. It is found in our observations on April 24 after the 7-minute appearance of the Q bright mode (Fig. 2), in the even briefer 1.4 minute long B-mode-like emission reported by Sobey et al. (2015) and also at the conclusion of hours-long B mode sequences (Rankin et al. 2018). Furthermore, in contrast to PSR B1822–09, no switching in the presence/absence of the PC or IP is found in the Q mode other than a reduction in intensity of these components roughly in proportion to the reduction in the MP intensity (Rankin et al. 2018).

Unfortunately no B-to-Q transitions were observed in our simultaneous X-ray and radio campaign, but it may be significant that the X-rays coinciding with the Q-bright mode of April 24 take about 100 minutes to diminish although only sporadic radio emission is detected (Fig. 5). It is possible that this happens at the end of every B mode sequence, indicating that radio emission is still occurring but undetectable. This would support the reasonable conjecture (see Section 8.2) that X-ray power is strongly correlated to the radio emission on every timescale down to the single pulses, suggesting that the detection of X-rays may be used to infer the presence of unseen radio emission. The low X-ray count rate, however, does not allow us to follow the null/burst/flicker pattern. Since in the radio emission this pattern is found on a wide range of timescales it is tempting to assume that the X-ray emission follows suit. Perhaps the reduction in the B mode X-rays during our on average 7-hours long observations (Fig. 4), and likely also visible in the observation by Becker et al. (2004) (Fig. 6), is also an indicator of the radio pattern existing on an even longer timescale.

A further difference between the radio behaviours of the two pulsars can be seen in the timescales and nature of their single-pulse modulation P_3 . In PSR B1822–09 the modulation timescales in both modes (Q mode $P_3 \sim 46P$ and B mode $\sim 70P$ (Latham et al. 2012)) can be seen as roughly compatible with the predicted value of the Ruderman & Sutherland (1975) carousel model and the emission is null-free. By contrast, PSR B0823+26 exhibits a B-

mode modulation of $P_3 \sim 5P$ that is significantly shorter, and, as noted above, appears as a burst rather than a simple smooth cycle. This was originally pointed out by Romani et al. (1992), who calculated a low fractal dimension for the attractor present in the chaotic null/burst behaviour. The modulation may therefore have a different physical origin to the carousel-based ‘drift’ phenomenon found in other (often near-aligned) pulsars such as PSR B0943+10. It is not impossible that the burst pattern persists in the Q mode but the weakness of the radio emission makes it undetectable.

It is interesting to speculate that in PSR B0823+26 we are not seeing ‘true’ mode-changing but the sudden appearance of strong bursts whose intensity follows a self-similar (*i.e.* fractal) distribution over a wide range of timescales. Thus what we identify as Q mode is simply emission largely hidden by our inability to detect it. Such systems are sometimes identified as exhibiting self-organised criticality (SOC) found in non-linear slowly-driven non-equilibrium systems such as avalanche theory (Bak et al. 1987) and may underlie the Rotating-Radio-Transient (RRAT) phenomenon (McLaughlin et al. 2006) that the Q mode strongly resembles².

If this picture is correct, then the sudden switches between two well-defined and null-free modes found in PSR B1822–09 and other pulsars (including PSR B0943+10) are a very different phenomenon to what we find in PSR B0823+26. However, caution is necessary since SOC systems are often characterised by power-law distributions, and while this was found to be the case in the weak Q-mode distributions analysed by Sobey et al. (2015), these authors found the B mode emission to be better modelled by log-normal statistics. Clearly further study of our longer radio observations could be used to investigate this.

Some years ago it was pointed out by Weltevrede et al. (2006a) that the middle-aged (X-ray detected) pulsar PSR B0656+17 simultaneously exhibited two types of radio emission, one of which was ‘spiky’ and would have been observed as RRAT emission if the pulsar was located at a greater distance. This implies the risk that the level of radio detectability determines the classification of the pulsar’s apparent mode rather than its intrinsic nature. Pursuing this argument, it is interesting to compare PSR B0823+26 to PSR J1752+2359, a pulsar which bears a close resemblance to PSR B0823+26 both in its emission behaviour and basic parameters ($P=0.4s$, $\tau \sim 10$ Myr, weak magnetic field $\sim 5 \times 10^{11}$ G), but is only in its burst state for little more than 10% of the time. The burst sequences have a structure similar to those described above for PSR B0823+26 and occasional strong inter-burst pulses are found to appear at random among the long ‘nulls’ (see Figures 7 and 11 of Gajjar et al. (2014)). However, this pulsar is located ten times further away than PSR B0823+26 (3 kpc compared with 0.3 kpc) which may simply make many bursts impossible to detect.

If PSR B0823+26 is a different kind of pulsar to PSR B1822–09, how do we account for this physically? A pulsar is generally considered to exist in a vacuum and its diverse radio phenomena, including mode changing, result entirely from non-linear interactions between the magnetosphere and the polar cap. This may well be the case for PSR B1822–09. However, the self-similar behaviour of PSR B0823+26 over many timescales, if it can be confirmed, suggests a different scenario.

The best-known example of a SOC system displays avalanches of different magnitudes being triggered by a light but

² Not all systems reach a high degree of criticality: in an investigation of the time series of 17 pulsars only one (PSR B1828–11) was found to possess clear chaotic behaviour (Seymour & Lorimer 2013).

steady rain of sand on a sandpile (Bak et al. 1987). By analogy, it is interesting to speculate that PSR B0823+26 is accreting material either from the interstellar medium through which it is passing, or, more specifically from fallback debris created by its own supernova. The idea of accretion by apparently isolated pulsars is not new (Wright 1979; Tsygan 1980; Cheng 1985; Luo & Melrose 2007; Cordes & Shannon 2008) and supposes that neutral hydrogen can pass through the bow shock of the extended magnetosphere and infiltrate the light cylinder where it becomes ionised and interferes with the pulsar’s emission either as an intermittent stream or via a disk. The former is a similar idea to the impact of the solar wind on the terrestrial ionosphere, leading to auroral effects, which indeed have been shown to follow SOC statistics (see review Aschwanden et al. (2016)).

If sufficient material is available, e.g. from supernova fallback material, it can give rise to a neutral accretion disk (Cordes & Shannon 2008) and in the context of PSR B0823+26 may help to explain the asymmetry of the X-ray pulse as being a combination of hot polar cap emission and cooler but more extended equatorial heating arising from the down flow of ionised material generated by the passing polar beam. The presence of an accretion disk may also account for the partial obscuration of the emission. Clearly, these ideas need to be worked out more carefully and they are presented to resolve the impasse between our observational results and existing polar cap theory.

9 CONCLUSIONS

We observed the radio-mode switching PSR B0823+26 for ~ 39 hours simultaneously in X-rays and the radio band and report the discovery of synchronous *correlated* X-ray & radio mode switching: when PSR B0823+26 is radio bright (B), we detect the pulsar in X-rays in the energy band 0.2–2 keV with a high pulsed fraction of 70–80% due to a sinusoidal pulse that is lagging the radio main pulse by ~ 0.2 in phase. During the radio-quiet or null mode (Q) we do not detect PSR B0823+26 in X-rays with an upper limit almost an order of magnitude lower than the reported flux in the B mode. This result is surprising, because the only pulsar for which synchronous X-ray & radio moding was found so far, PSR B0943+10, showed *anti-correlated* mode switches (Hermsen et al. 2013). The latter pulsar exhibits thermal pulsed as well as non-thermal unpulsed X-ray emission, both varying by a factor ~ 2 in flux between similar radio B and Q modes (Mereghetti et al. 2016).

PSR B0943+10 is classified as a nearly aligned rotator (near alignment of the magnetic and rotation axis) and PSR B0823+26 as a near-perpendicular rotator, but these pulsars have in common their broad thermal X-ray pulses with high pulsed fractions. Such high pulsed fractions can not be generated modelling blackbody emission isotropically emitted from a hot polar cap. For PSR B0823+26, we showed that its X-ray spectrum, pulse shape and pulsed fraction can be reproduced with a magnetized partially ionized hydrogen atmosphere model, with the two polar caps having the same temperatures but somewhat different sizes. However, this atmosphere-model fit to our X-ray data requires the angle between the rotation axis and line of sight direction to be $\sim 66^\circ$, in conflict with the accurately radio-derived value of $\sim 84^\circ$. Storch et al. (2014) applied a similar atmosphere model to the X-ray data of PSR B0943+10 and approximately reproduced also for this nearly aligned pulsar the pulse profile and high pulsed fraction, but in this case the radio-derived angles could be used in the model. In conclusion, we do not have an explanation yet for the

high X-ray pulsed fractions that is consistently in agreement with radio-derived parameters.

In this work we discovered, in addition to the synchronous X-ray & radio mode switching, a new type of X-ray variability: the average X-ray flux within B-mode intervals of duration ~ 7 hours varied by a factor $\pm 20\%$. We speculate that the X-ray generation follows very closely the variations in frequency and lengths of short radio nulls or short durations of weak emission seen during the B mode, possibly on time scales of even few pulses. This possibility offers interesting constraints on the interpretation of what is causing mode switching: are we dealing with a local or global magnetospheric phenomenon? A follow-up investigation of the available single-pulse radio data is required to investigate such a possible tight X-ray/radio correlation.

In our discussion on the possible nature of mode changing in PSR B0823+26, we discussed in detail the radio and X-ray characteristics of PSR B0823+26 compared to those of the also radio-mode switching PSR B1822–09. For the latter pulsar an earlier X-ray/radio campaign did not reveal synchronous moding (Hermsen et al. 2017). Both pulsars are near-perpendicular rotators. We are speculating that in PSR B0823+26 we are not seeing ‘true’ mode-changing but the sudden appearance of strong bursts whose intensities follow a self-similar (*i.e.* fractal) distribution over a wide range of timescales. Such a system could be identified as exhibiting self-organized criticality. In this context, we speculate that PSR B0823+26 is accreting material from a debris disk or the interstellar medium through which it is passing, to explain some of its X-ray characteristics. Further study of rotation-powered radio pulsars using simultaneous X-ray/radio data is needed to test and develop these various hypotheses.

ACKNOWLEDGMENTS

We thank the staff of *XMM-Newton*, GMRT, LOFAR and Lovell for making these observations possible. *XMM-Newton* is an ESA science mission with instruments and contributions directly funded by ESA member states and by NASA. GMRT is run by the National Centre for Radio Astrophysics of the Tata Institute of Fundamental Research. This paper is based (in part) on results obtained with International LOFAR Telescope (ILT) equipment, as part of project LC7-014. LOFAR is the Low Frequency Array designed and constructed by ASTRON. It has observing, data processing, and data storage facilities in several countries, that are owned by various parties (each with their own funding sources), and that are collectively operated by the ILT foundation under a joint scientific policy. The ILT resources have benefitted from the following recent major funding sources: CNRS-INSU, Observatoire de Paris and Université d’Orléans, France; BMBF, MIWF-NRW, MPG, Germany; Science Foundation Ireland (SFI), Department of Business, Enterprise and Innovation (DBEI), Ireland; the Netherlands Organisation for Scientific Research (NWO), The Netherlands; The Science and Technology Facilities Council, UK7. Pulsar research at the Jodrell Bank Centre for Astrophysics and the observations using the Lovell telescope is supported by a consolidated grant from the STFC in the UK. We acknowledge the use of the international LOFAR stations operated by the MPIfR (DE601), the Nançay Radio Observatory, operated by Paris Observatory, associated with the French Centre National de la Recherche Scientifique and Université d’Orléans (FR606). ASTRON and SRON are supported financially by NWO. JMR acknowledges funding from a NASA Space Grant. JWTH acknowledges funding from an NWO Vidi fellowship and from

the European Research Council under the European Union's Seventh Framework Programme (FP/2007-2013) / ERC Starting Grant agreement nr. 337062 ("DRAGNET"). WCGH acknowledges support from STFC in the UK through grant number ST/M000931/1, and appreciates use of computer facilities at the Kavli Institute for Particle Astrophysics and Cosmology. GW thanks the University of Manchester to granting Visitor status. DM acknowledges funding from the grant "Indo-French Centre for the Promotion of Advanced Research, CEFIPRA".

REFERENCES

- Antonopoulou D., Vasilopoulos G., Espinoza C. M., 2016, *The Astronomer's Telegram*, [9282](#)
- Archibald R. F., Kaspi V. M., Tendulkar S. P., Scholz P., 2016, *ApJ*, [829](#), L21
- Aschwanden M. J., et al., 2016, *Space Sci. Rev.*, [198](#), 47
- Backer D. C., 1973, *ApJ*, [182](#), 245
- Backer D. C., Boriakoff V., Manchester R. N., 1973, *Nature Physical Science*, [243](#), 77
- Bak P., Tang C., Wiesenfeld K., 1987, *Physical Review Letters*, [59](#), 381
- Basu R., Mitra D., 2018, *MNRAS*, [476](#), 1345
- Becker W., Weisskopf M. C., Tennant A. F., Jessner A., Dyks J., Harding A. K., Zhang S. N., 2004, *ApJ*, [615](#), 908
- Beloborodov A. M., 2002, *ApJ*, [566](#), L85
- Bilous A. V., et al., 2016, *A&A*, [591](#), A134
- Bogdanov S., 2016, *European Physical Journal A*, [52](#), 37
- Bogdanov S., Rybicki G. B., Grindlay J. E., 2007, *ApJ*, [670](#), 668
- Buccheri R., et al., 1983, *A&A*, [128](#), 245
- Camilo F., Ransom S. M., Chatterjee S., Johnston S., Demorest P., 2012, *ApJ*, [746](#), 63
- Cheng A. F., 1985, *ApJ*, [299](#), 917
- Contopoulos I., 2005, *A&A*, [442](#), 579
- Cordes J. M., Lazio T. J. W., 2002, *ArXiv Astrophysics e-prints*,
- Cordes J. M., Shannon R. M., 2008, *ApJ*, [682](#), 1152
- Deshpande A. A., Rankin J. M., 2001, *MNRAS*, [322](#), 438
- Dickey J. M., Lockman F. J., 1990, *ARA&A*, [28](#), 215
- Everett J. E., Weisberg J. M., 2001, *ApJ*, [553](#), 341
- Fowler L. A., Wright G. A. E., 1982, *A&A*, [109](#), 279
- Fowler L. A., Wright G. A. E., Morris D., 1981, *A&A*, [93](#), 54
- Gajjar V., Joshi B. C., Wright G., 2014, *MNRAS*, [439](#), 221
- Gavril F. P., Gonzalez M. E., Gotthelf E. V., Kaspi V. M., Livingstone M. A., Woods P. M., 2008, *Science*, [319](#), 1802
- Goodwin S. P., Mestel J., Mestel L., Wright G. A. E., 2004, *MNRAS*, [349](#), 213
- Hermsen W., et al., 2013, *Science*, [339](#), 436
- Hermsen W., et al., 2017, *MNRAS*, [466](#), 1688
- Ho W. C. G., 2007, *MNRAS*, [380](#), 71
- Ho W. C. G., 2014, in Petit P., Jardine M., Spruit H. C., eds, *IAU Symposium Vol. 302, Magnetic Fields throughout Stellar Evolution*. pp 435–438 ([arXiv:1311.5583](#)), doi:10.1017/S1743921314002683
- Ho W. C. G., Potekhin A. Y., Chabrier G., 2008, *ApJS*, [178](#), 102
- Kalberla P. M. W., Burton W. B., Hartmann D., Arnal E. M., Bajaja E., Morras R., Pöppel W. G. L., 2005, *A&A*, [440](#), 775
- Kramer M., Lyne A. G., O'Brien J. T., Jordan C. A., Lorimer D. R., 2006, *Science*, [312](#), 549
- Latham C., Mitra D., Rankin J., 2012, *MNRAS*, [427](#), 180
- Lorimer D. R., Lyne A. G., McLaughlin M. A., Kramer M., Pavlov G. G., Chang C., 2012, *ApJ*, [758](#), 141
- Luo Q., Melrose D., 2007, *MNRAS*, [378](#), 1481
- Lyne A., Hobbs G., Kramer M., Stairs I., Stappers B., 2010, *Science*, [329](#), 408
- McLaughlin M. A., et al., 2006, *Nature*, [439](#), 817
- Mereghetti S., et al., 2016, *ApJ*, [831](#), 21
- Pavlov G. G., Shibano Y. A., Ventura J., Zavlin V. E., 1994, *A&A*, [289](#), 837
- Pechenick K. R., Ftaclas C., Cohen J. M., 1983, *ApJ*, [274](#), 846
- Rankin J. M., Suleymanova S. A., 2006, *A&A*, [453](#), 679
- Rankin J. M., Olszanski T., Wright G. A. E., 2018, In preparation
- Rathnasree N., Rankin J. M., 1995, *ApJ*, [452](#), 814
- Romani R. W., 1987, *ApJ*, [313](#), 718
- Romani R. W., Rankin J. M., Backer D. C., 1992, in Hankins T. H., Rankin J. M., Gil J. A., eds, *IAU Colloq. 128: Magnetospheric Structure and Emission Mechanics of Radio Pulsars*. p. 326
- Ruderman M. A., Sutherland P. G., 1975, *ApJ*, [196](#), 51
- Seymour A. D., Lorimer D. R., 2013, *MNRAS*, [428](#), 983
- Shibanov I. A., Zavlin V. E., Pavlov G. G., Ventura J., 1992, *A&A*, [266](#), 313
- Sobey C., et al., 2015, *MNRAS*, [451](#), 2493
- Stappers B. W., et al., 2011, *A&A*, [530](#), A80
- Storch N. I., Ho W. C. G., Lai D., Bogdanov S., Heinke C. O., 2014, *ApJ*, [789](#), L27
- Strüder L., et al., 2001, *A&A*, [365](#), L18
- Sulejmanova S. A., Izvekova V. A., 1984, *Azh*, [61](#), 53
- Swarup G., Ananthakrishnan S., Kapahi V. K., Rao A. P., Subrahmanya C. R., Kulkarni V. K., 1991, *Current Science*, Vol. 60, NO.2/JAN25, P. 95, 1991, [60](#), 95
- Szary A., Melikidze G. I., Gil J., 2015, *MNRAS*, [447](#), 2295
- Timokhin A. N., 2010, *MNRAS*, [408](#), L41
- Tsygan A. I., 1980, *Soviet Ast.*, [24](#), 44
- Turner M. J. L., et al., 2001, *A&A*, [365](#), L27
- Verbiest J. P. W., Weisberg J. M., Chael A. A., Lee K. J., Lorimer D. R., 2012, *ApJ*, [755](#), 39
- Weltevrede P., Edwards R. T., Stappers B. W., 2006a, *A&A*, [445](#), 243
- Weltevrede P., Stappers B. W., Rankin J. M., Wright G. A. E., 2006b, *ApJ*, [645](#), L149
- Weltevrede P., Stappers B. W., Edwards R. T., 2007, *A&A*, [469](#), 607
- Wright G. A. E., 1979, *Nature*, [280](#), 40
- Yao J. M., Manchester R. N., Wang N., 2017, *ApJ*, [835](#), 29
- Young N. J., Stappers B. W., Weltevrede P., Lyne A. G., Kramer M., 2012, *MNRAS*, [427](#), 114
- Zou W. Z., Hobbs G., Wang N., Manchester R. N., Wu X. J., Wang H. X., 2005, *MNRAS*, [362](#), 1189
- van Haarlem M. P., et al., 2013, *A&A*, [556](#), A2